Journal of Sound and Vibration (2002) **252**(2), 281–315
doi:10.1006/jsvi.2001.3962, available online at http://www.idealibrary.com on IDEAL®

EXPERIMENTAL AND THEORETICAL INVESTIGATION OF THE LINEAR AND NON-LINEAR DYNAMIC BEHAVIOUR OF A GLARE 3 HYBRID COMPOSITE PANEL

B. Harras

Laboratoire de Modélisation Numérique et Analyse des Structures, LAMNAS, FST de Fès-Saiss,
Route d'Immouzer, BP 2202 Fès, Morocco

R. Benamar

Laboratoire d'Etudes et de Recherches en Simulation, Instrumentation et Mesure, LERSIM,
E.G.T, Ecole Mohammadia d'Ingénieurs, Université Mohammed V, BP 765 Agdal, Rabat, Morocco

and

R. G. White

Department of Aeronautics and Astronautics, University of Southampton, Highfield,
Southampton S017 1BJ, England

(*Received* 5 *March* 2001, *and in final form* 14 *August* 2001)

A theoretical model based on Hamilton's principle and spectral analysis is used to study the non-linear free vibration of hybrid composite plates made of Glare 3, a new aircraft structural material. It consists of alternating layers of metal- and fibre-reinforced composites. In previous work, the theoretical model has been used to calculate the first non-linear mode of fully clamped rectangular composite fibre-reinforced plastic (CFRP) laminated plates. This study concerns determination of the linear dynamic properties of the Glare 3 hybrid composite rectangular panel (G3HCRP) such as natural frequencies and mode shapes. The theoretical model is used to calculate the fundamental non-linear mode shape and associated flexural behaviour of the fully clamped G3HCRP. A series of experimental investigations have been conducted using a G3HCRP in order to determine linear dynamic properties. The response due to random excitation was investigated and the experimental measurements are analyzed and discussed. Comparisons are made with finite element predictions and response estimates given by the ESDU method, the latter being a "design guide" approach used by industry. Concerning the non-linear analysis, the results are given for various plate aspect ratios and vibration amplitudes, showing a higher increase of the induced bending stress near the clamps at large deflections. Comparisons between the dynamic behaviour of an isotropic plate and G3HCRP at large vibration amplitudes are presented and good results are obtained.

1. INTRODUCTION

The use of composite materials as an alternative to traditional metal materials is becoming widespread. The main technological advantages of these materials are low weight, high strength and high stiffness, environmental resistance and long life. Composites technology will play an increasingly important role in the aircraft industry in the future [1]. It is predicted that there will be a considerable demand for aircraft structures which will be manufactured from advanced composite materials [2]. The carbon-fibre-reinforced plastic (CFRP) presents remarkable specific stiffness and a better fatigue performance when compared with other composite materials and metals. Because of such superior priorities and of the very high stiffness-to-weight ratio, which is a very important parameter in aircraft design, CFRP has a very good performance. However, its impact resistance is inferior to aluminium alloy [3].

New materials have been developed which combine the advantages of both metal and the fibre-reinforced composite. Glare 3 is one of these materials. It was developed by Delft University of Technology. It is a type of material known as fibre-reinforced metal laminates (FML). Glare 3 is a hybrid composite material consisting of alternating layers of metal and fibre-reinforced composites. This material has many properties that make it particularly attractive to the aerospace industry. Glare 3 presents many advantages over reinforced plastic: it has an excellent corrosion resistance, a good fire resistance, an impact damage tolerance and high resistance to fatigue [4–7]. Glare 3 also has direct cost and weight advantages: it is up to three times less expensive than other advanced composites, whilst retaining at least the same weight-saving potential [8].

In service, aircraft structures are subjected to dynamic loading. The correct and effective use of composite materials such as CFRP and FML requires more complex analysis techniques in order to predict accurately the dynamic response of such structures to external loading, especially in severe environments, which may induce geometrically non-linear behaviour [9]. Considerable research has been carried out on the non-linear dynamic response of beams, homogeneous and composite plates and shells. A summary of existing knowledge in the field of vibrations of plates and shells has been presented in references [10–16]. In reference [17], an excellent review of the technical literature on the acoustic fatigue of beams and plates has been presented. Research on the dynamics of isotropic and composite plates has been presented in references [18–22]. The free and forced linear and non-linear vibration analysis of symmetrically laminated rectangular plates has been investigated in references [23–28] using the hierarchical finite element method.

In a series of papers [29–39], a theoretical model based on Hamilton's principle and spectral analysis has been developed and used to study the non-linear free and steady state periodic forced vibration of beams, and the non-linear free vibration of shells and homogeneous and composite plates. In reference [32], the model developed in reference [29] has been extended to the non-linear free vibration of cylindrical shells. The effects of large vibration amplitudes on the first and second coupled transverse–circumferential mode shapes of isotropic circular cylindrical shells of infinite length have been examined. In reference [35], this model was used to calculate the second non-linear mode of fully clamped homogeneous rectangular plate for various values of the aspect ratio, and to analyze the effect of non-linearity on the induced bending stresses. In reference [36], the model presented in references [29–31] was adapted to study the non-linear steady state forced periodic response of C–C and S–S beams; the results obtained were close to those obtained by other methods. More recently, this method has been extended to the free vibration of clamped circular plates and C–C–C–SS plates [37–38]. Good agreement has been found in each case when compared with previous published works. In reference [39], the geometrically non-linear free vibration of symmetrically laminated rectangular plates with the fully clamped boundary conditions has been examined both experimentally and theoretically. The model was validated by comparison with experimental results.

In the present work, experimental investigations have been performed in an attempt to understand the dynamic behaviour of the Glare 3 hybrid composite rectangular panel (G3HCRP) tested. The fully clamped panel was driven by random excitation using a coil and magnet shaker. These tests allow determination of the dynamic properties of the panel and the damping. The results are presented in terms of the basic function components of the mode shapes with their associated natural frequencies and damping. The experimental data have been analyzed using the modal analysis criterion (MAC) in order to evaluate the degree of correlation between the modes and validity of the experimental data. Comparison between theoretical results obtained from the solution of the linear eigenvalue problem, finite element predictions and response estimates obtained by the ESDU method has been made. The classical linear eigenvalue problem, based on the Rayleigh–Ritz method, in which products of x and y beam functions are used as basic functions, has been solved in order to obtain the G3HCRP theoretical first five natural frequencies and corresponding mode shapes. A software called STAR has been used to obtain the linear mode shapes of the G3HCRP from the experimental data.

The geometrically non-linear free vibration of G3HCRP with fully clamped boundary conditions has been also examined. Fully clamped boundaries have been considered here because they are adequate for modelling many real panel-type situations, such as aircraft wing panels [40], and it is more realistic to attempt to achieve these in practice, compared with simply supported boundaries, for experimental measurements, as discussed in reference [35]. Results are given for various plate aspect ratios and vibration amplitudes. The comparison of the fundamental non-linear mode shape of the G3HCRP with that of an isotropic plate has shown that the G3HCRP exhibits more non-linearity than an isotropic plate of the same thickness. Comparisons of the change in natural frequency at large vibration amplitudes, between G3HCRP and isotropic plates are presented. Some experimental measurements for the first non-linear mode shape are also reported and discussed. The second and higher non-linear mode shapes will be presented later.

2. LINEAR DYNAMIC PROPERTIES OF THE GLARE 3 COMPOSITE PANEL

2.1. INTRODUCTION

As Glare 3 which is considered in the present work is a new material, it was necessary to determine its linear dynamic characteristics before examining the geometrically non-linear behaviour. In this section, experimental and numerical investigations of the linear dynamic properties of the G3HCRP are presented. This material, in the form of a rectangular plate, was tested experimentally using electrodynamic point excitation. The G3HCRP was driven by random excitation using a coil and magnet shaker in the frequency range 0–700 Hz, which included the first five natural frequencies of the panel. The data taken from the experiments have been analyzed and compared with theoretical predictions.

The purpose of this study was determination of basic structural properties such as the mode shapes, natural frequencies and damping.

2.2. EXPERIMENTAL INVESTIGATIONS

2.2.1. *Description of the glare* 3 *panel*

The G3HCRP tested was designed and manufactured by British Aerospace Airbus Ltd. It was in the form of a rectangular plate, with dimensions $0{\cdot}45 \times 0{\cdot}3$ m. The material used was a five-layered aluminium alloy/glass-reinforced plastic (GRP) material, with three layers of aluminium alloy (0·3 mm thickness each) and two-layers of composite constituent glass fibre/epoxy matrix (0·25 mm each). The S2-glass fibres of the G3HCRP were oriented in two

Table 1

Lay-up of Glare 3 hybrid composite material

Lay-up	Materials	Layer thickness (mm)	Fibre orientation	
			Glare 2	Glare 3
—— 1	2423-T3	0·30		
—— 2	Glass composite	0·25	UD[†] 0°	CP[‡] 0/90°
—— 3	2423-T3	0·30		
—— 4	Glass composite	0·25	UD 0°	CP 0/90°
—— 5	2324-T3	0·30		

[†] UD—unidirectional. [‡] CP—cross-ply.

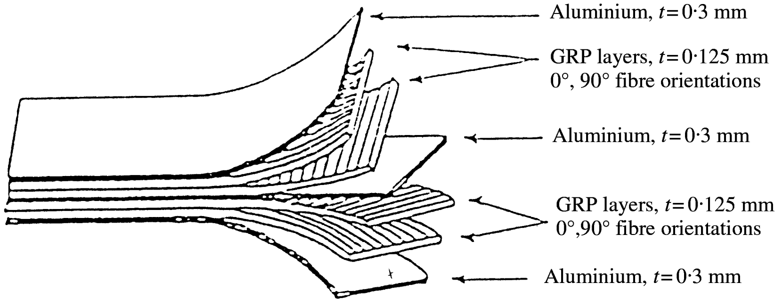

Figure 1. Glare 3 hybrid laminate lay-up.

perpendicular directions, that is a cross-ply (0/90) orientation. The lay-up of Glare 3 is listed in Table 1 and the construction of this material is shown in Figure 1.

The material properties of G3HCRP are listed below. Data were supplied by the manufacturer of the material. The fibre volume fraction of the GRP is unknown as it was not specified by the manufacturer.

- *Aluminium alloy layer*:

Modulus of elasticity : $E = 72{\cdot}39$ GPa
The Poisson ratio : $v = 0{\cdot}33$
Density : $\rho = 2700$ kg/m^3

- *Glass fibre composite layer–cross plied* (*Glare* 3):

Modulus of elasticity (longitudinal) : $E_x = 31{\cdot}17$ GPa The Poisson ratio : $v_{xy} = 0{\cdot}098$
Modulus of elasticity (transverse) : $E_y = 31{\cdot}17$ GPa : $v_{yz} = 0{\cdot}0575$
Modulus of elasticity (transverse) : $E_z = 9{\cdot}412$ GPa : $v_{xz} = 0{\cdot}0575$
Shear modulus : $G_{xy} = 5{\cdot}548$ GPa Density : ρ =2000 kg/m^3

2.2.2. *Experimental set-up*

The excitation force was a stationary random signal. This type of signal has statistical characteristics which do not change with time [41]. Low-level stationary random excitation was used in order to characterize the linear dynamic properties of the G3HCRP by determining the first five mode shapes and natural frequencies. The results are presented in terms of the mode shapes with their corresponding natural frequencies and modal damping

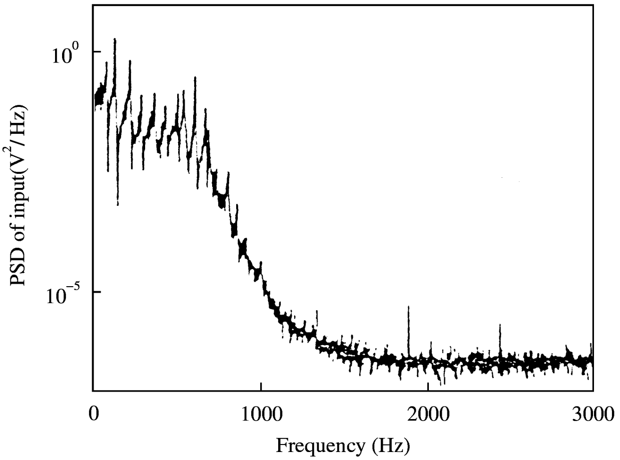

Figure 2. Spectral density of the excitation force for the modal tests of the Glare 3 hybrid composite panel.

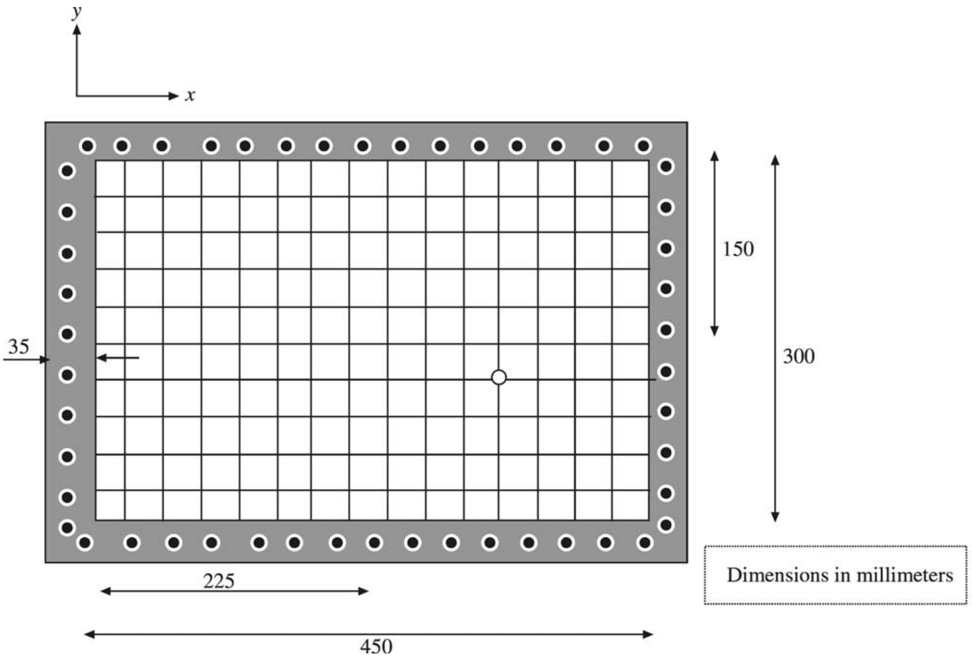

Figure 3. Measurements grids for the Glare 3 hybrid composite panel. The position of the excitation point is indicated by a circle.

ratios. The panel was driven by a random excitation force obtained by means of a coil and magnet. The spectral density (PSD) of the excitation force is given in Figure 2 which shows an almost constant spectrum in the range 0–700 Hz. A light coil was attached to a light screw, which was glued to the panel. The coil protruded into the flux gap of an annular permanent magnet, thus forming an electrodynamic exciter, which imposed no added stiffness and little additional mass on the panel. The excitation point was chosen as shown in Figure 3. This choice was made in such a manner that the first five modes would be

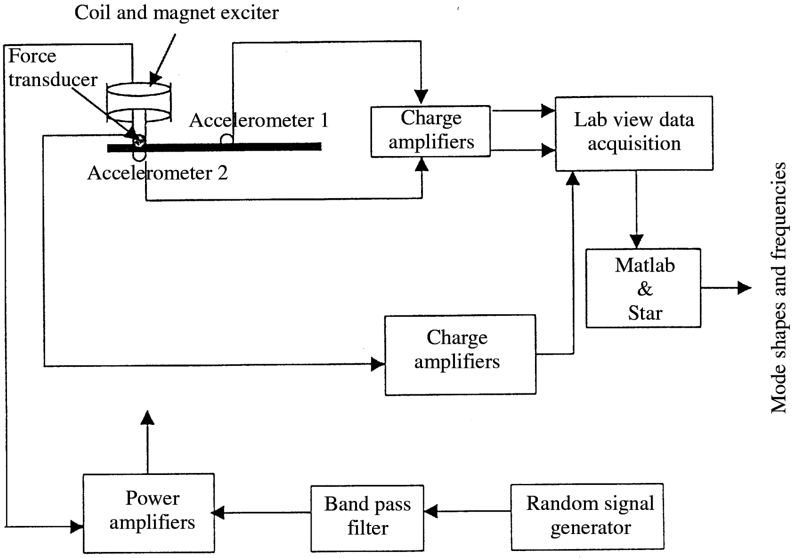

Figure 4. Instrument arrangement for the modal tests of the Glare 3 hybrid composite panel

excited significantly. The response of the panel at the 126 measuring points across the surface of the panel indicated in Figure 3, and for various levels of the excitation force, was measured by an accelerometer, and a force transducer was used to measure the excitation signal (see calibration of the measurement system in Appendix B). The instrument arrangement for the modal tests of the Glare 3 hybrid composite panel is shown in Figure 4. This allowed production of a series of transfer functions between the excitation and the response. The modal parameters have been extracted using a modal analysis software called STAR.

2.2.3. *Modal test linearity check*

Modal testing was used to determine the natural frequencies and mode shapes of the plate considered. The validity of this method is restricted to the range of vibration amplitudes within which the behaviour remains linear. It was therefore necessary to check this condition. For a linear system, the response of the panel is linearly related to the increase of the excitation level. Thus the response increases proportionally but the transfer function, which is the ratio between input and output, must remain unchanged. To ensure that the panel was vibrating in its linear range during the modal tests, the panel was driven at three different excitation levels and the response at the closest point to the driving point was measured. Figure 5 shows the measured transfer and coherence functions at three driving force levels (r.m.s.) of 0·028, 0·054 and 0·071 N. It can be seen that the panel responded linearly to the driving force in the range considered. In the modal tests performed, the driving force was kept within this range.

2.2.4. *Modal tests results*

This section concerns the modal tests results. Measurements were made at a total of 126 points on the surface of the panel. In this study, the highest frequency of interest, based on theoretical predictions of the first five natural frequencies of G3HCRP, was below 400 Hz. So the time signals were low-pass filtered with a cut-off frequency of 700 Hz. A sampling

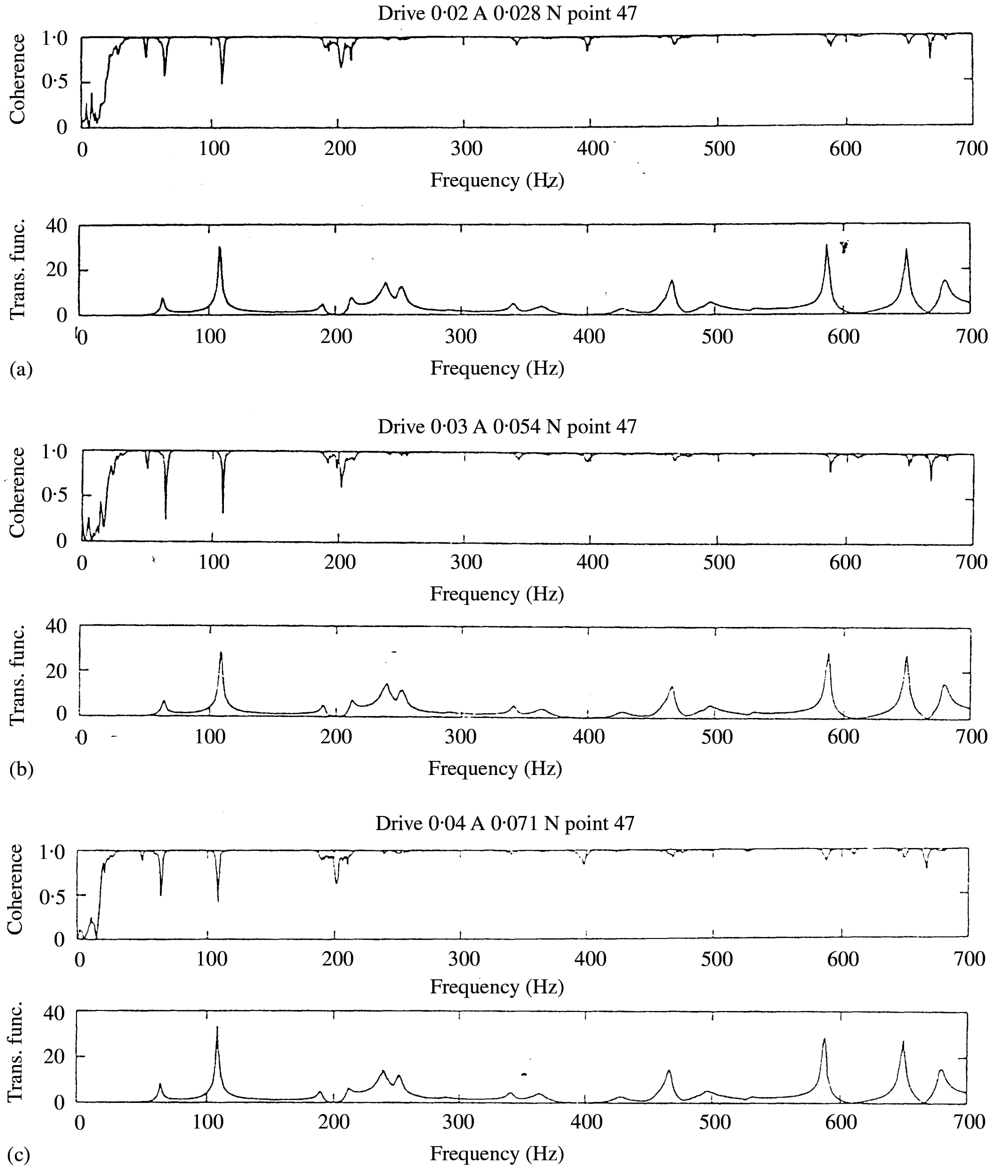

Figure 5. Modal test linearity check of the Glare 3 hybrid composite panel (upper—coherence; lower—transfer function): (a) driving force 0·028 (r.m.s.); (b) driving force 0·054 (r.m.s.); (c) driving force 0·071 (r.m.s.).

rate of 7000 Hz, 10 times the maximum frequency present in the data, was selected in order to preserve accurate frequency information when digitally sampling the analogue signal, and to avoid an aliasing phenomenon. Selecting a record length of 7 s and a sampling rate of 7000 Hz, yield a total number of samples of 49 000. The data were processed using the mathematical signal processing programs in MATLAB to produce the transfer and coherence functions. Two examples of the transfer and coherence functions are shown in Figure 6. Figure 6(a) corresponds to measured data at a point very close to the driving point, and Figure 6(b) corresponds to a point of 21 cm from the the driving point. The STAR modal analysis system was used to extract the modal parameters. STAR employs

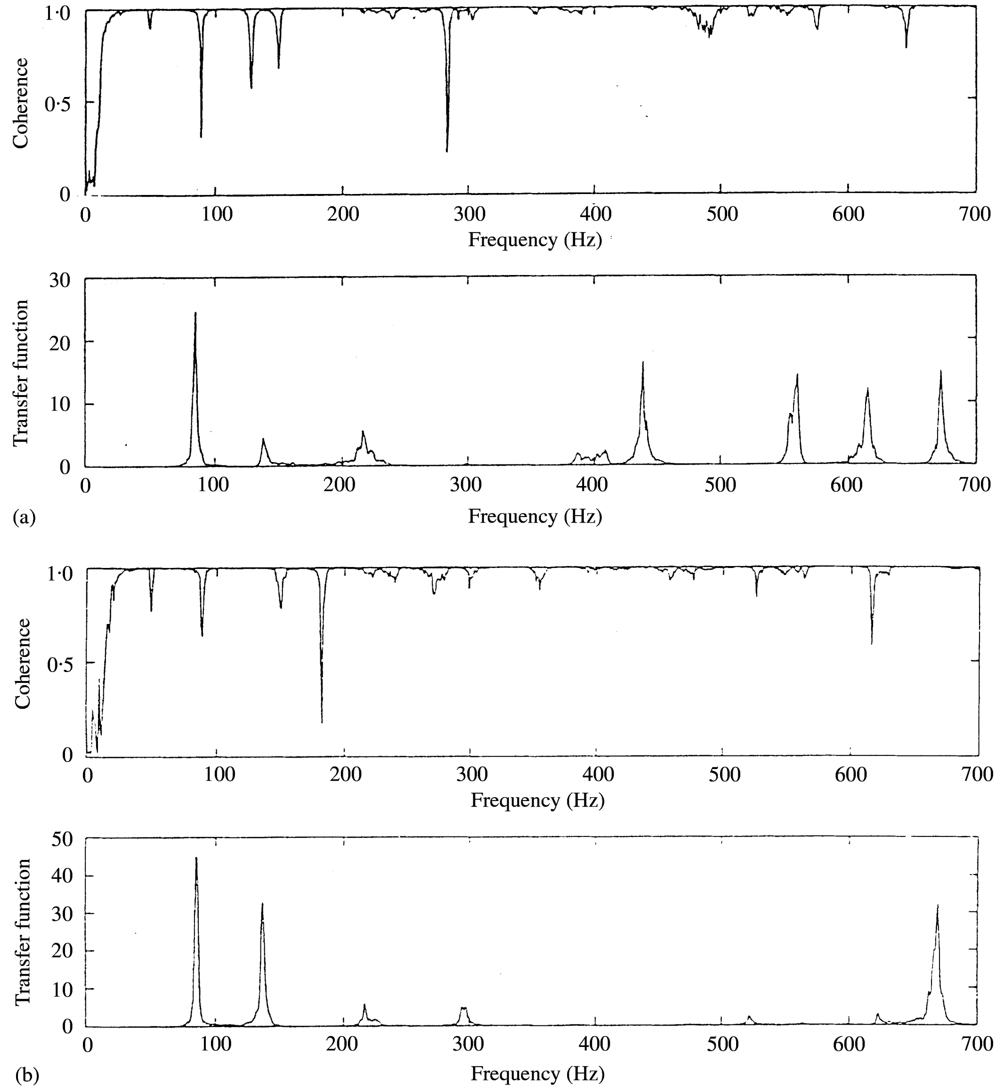

Figure 6. Two examples for the transfer (lower) and (upper) coherence functions during the modal tests of the Glare 3 hybrid composite panel (upper—coherence; lower—transfer function): (a) measurements point near the driving point; (b) measurements point far from the driving point.

measured transfer functions to estimate the mode shapes and modal damping at specified resonance frequencies.

The results are given in terms of mode shapes, natural frequencies and modal damping. Figure 7 shows comparisons of the first five mode shapes obtained from experimental measurements and those obtained from finite element analysis [42]. The overall viscous average damping ratio across the modal frequencies measured for the G3HCRP was 0·7%.

To evaluate the degree of correlation between the modes, the modal assurance criterion (MAC) data were used in order to check the orthogonality of the modes. If two modes are identical or proportional, the MAC = 1, and if two modes are unrelated the MAC = 0. This implies that the MAC table should have value 1 along the diagonal line and 0 for the remainder of the data. For good experimental data, values close to 1 or 0 are expected. The

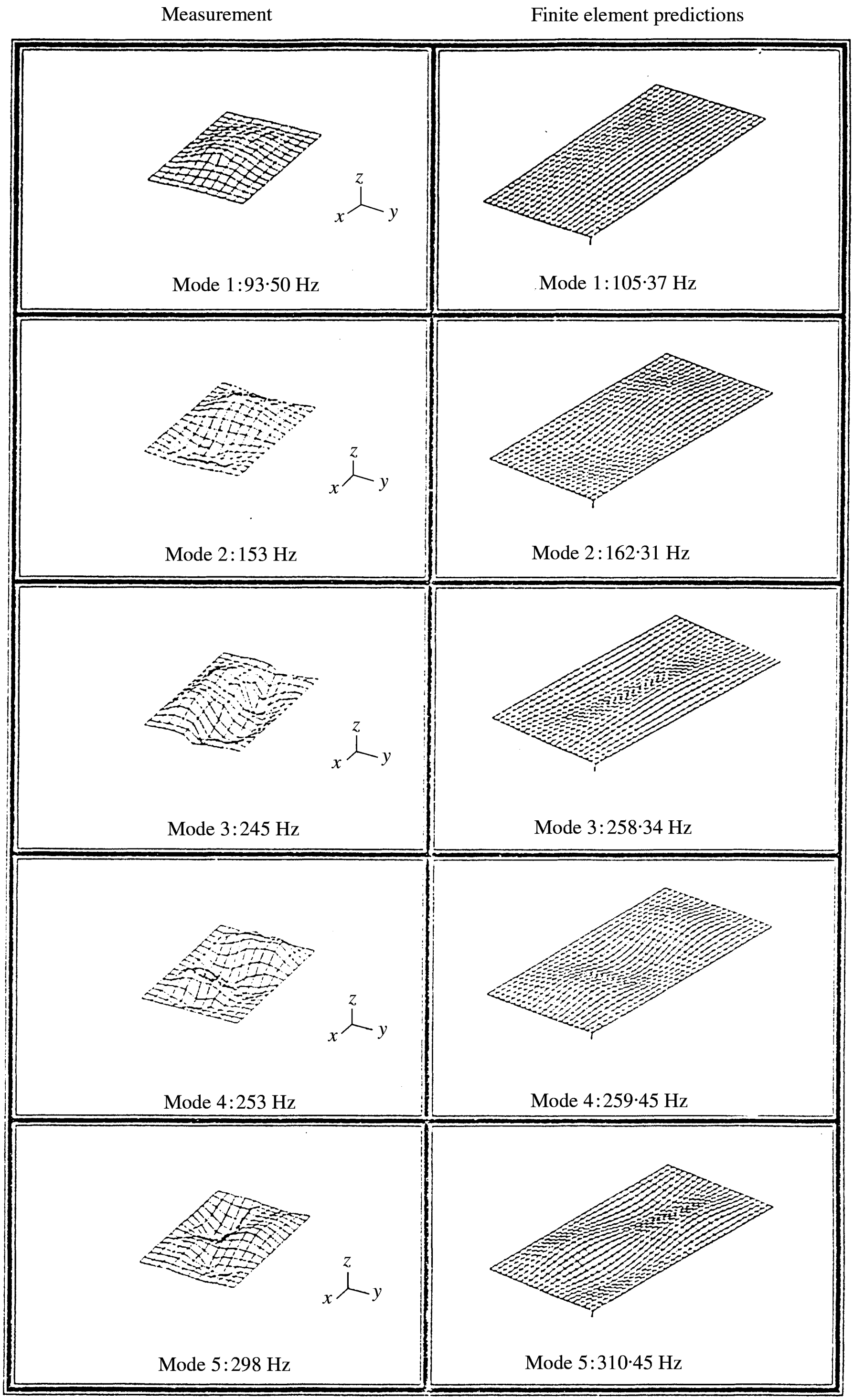

Measurement

Finite element predictions

Mode 1:93·50 Hz

Mode 1:105·37 Hz

Mode 2:153 Hz

Mode 2:162·31 Hz

Mode 3:245 Hz

Mode 3:258·34 Hz

Mode 4:253 Hz

Mode 4:259·45 Hz

Mode 5:298 Hz

Mode 5:310·45 Hz

Figure 7. Comparison between finite element predictions [42] and experimental results.

TABLE 2

Modal assurance criterion (MAC) results: correlation between the modes

	Mode 1	Mode 2	Mode 3	Mode 4	Mode 5
Mode 1	1·00	0·00	0·00	0·00	0·00
Mode 2	0·00	1·00	0·00	0·00	0·00
Mode 3	0·00	0·00	1·00	0·00	0·00
Mode 4	0·00	0·00	0·00	1·00	0·00
Mode 5	0·00	0·00	0·00	0·00	1·00

TABLE 3

Comparison of the experimental natural frequencies results and those obtained by ESDU method, finite element predictions and present numerical results

Mode number	ESDU (Hz)	Finite element (Hz)	Present numerical results (Hz)	Experimental (Hz)
(1·1)	105·60	105·37	104·64	93·50
(2·1)	162·90	162·31	161·26	153
(1·2)	259·40	258·34	256·63	245
(3·1)	260·30	259·13	257·52	253
(2·2)	311·90	310·45	308·63	298

MAC table obtained for the tests carried out on the G3HCRP is listed in Table 2. For all modes, the results are satisfactory.

2.3. NUMERICAL STUDIES

In order to obtain theoretically the first five natural frequencies of a fully clamped G3HCRP, the classical linear modal analysis free vibration equation based on the Raleigh–Ritz method, was used. The equation is given by [43]

$$a_i k^*_{ir} = a_i \omega^{*^2} m^*_{ir}, \quad i = 1, \ldots, n \qquad (1)$$

in which k^*_{ij} and m^*_{ij} are general terms of the non-dimensional classical rigidity and mass matrices and the usual summation convention for repeated indexes is used (see Appendix A for details).

The basic functions used in the non-linear rectangular plate analysis were obtained as products of x- and y-clamped–clamped beam functions. These functions which satisfy all the fully clamped theoretical boundary conditions, i.e., zero displacement and zero slope along the four plate edges, have been used in previous studies on fully clamped rectangular plate vibration [10] and have been demonstrated in many cases to be appropriate for the determination of plate natural frequencies and mode shapes [13].

Calculations were made using 36 basic functions obtained as products of the first six clamped–clamped beam functions, leading to square mass and rigidity matrices of dimension 36. The eigenvalue problem (1) has been solved using MATLAB software. Table 3 shows the comparison between the first five natural frequencies obtained experimentally, and those obtained theoretically, based on finite element predictions and the ESDU method [42]. It can be seen that the experimental values are reasonably close to the theoretical ones (the difference does not exceed 9·8%) and that the theoretical values are always greater than the experimental data, which is to be expected because of lack of perfect clamping in the experiments and possible over estimation by the Rayleigh–Ritz method.

In the next section, the extension of the Rayleigh–Ritz method to geometrically non-linear vibration, developed in reference [39], will be used to investigate the fundamental non-linear mode shape and associated amplitude-dependent resonant frequencies of a fully clamped G3HCRP.

3. THEORETICAL INVESTIGATIONS OF THE EFFECTS OF LARGE VIBRATION AMPLITUDES ON THE FUNDAMENTAL MODE SHAPE OF A FULLY CLAMPED G3HCRP

The purpose of this section is to apply the theory developed in reference [30] to calculate the non-linear fundamental mode shape of a rectangular G3HCRP. In this part of the paper, a brief review of the theory of the non-linear free response problem, corresponding to large vibration amplitudes of composite rectangular plates, developed in reference [39], is presented. Numerically results are given for various plate aspect ratios and vibration amplitudes. The effect of non-linearity on the induced bending stress patterns is also analyzed.

3.1. THEORETICAL FORMULATION

Consider an N-layer laminated composite with length a, width b and thickness H, shown in Figure 8, with the principal axes coinciding with the Cartesian co-ordinate system (x, y, z) such that the z-axis is perpendicular to the plane defined by x and y. W is the transverse

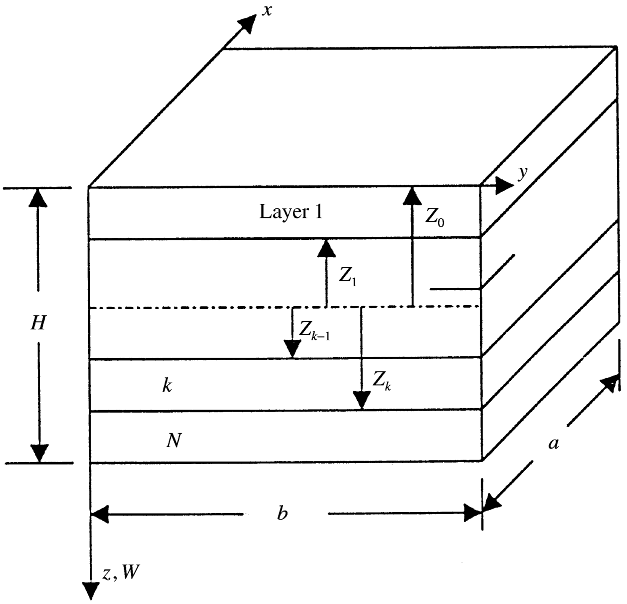

Figure 8. Geometry of laminated plate.

displacement. Based on the classical plate theory [44], the equation for the strain for large deflections can be expressed as [45]

$$\{\boldsymbol{\varepsilon}\} = \{\boldsymbol{\varepsilon}^0\} + z\{\boldsymbol{\kappa}\} + \{\boldsymbol{\lambda}^0\} \tag{2}$$

in which $\{\boldsymbol{\varepsilon}^0\}$, $\{\boldsymbol{\kappa}\}$ and $\{\boldsymbol{\lambda}^0\}$ are given by

$$\{\boldsymbol{\varepsilon}^0\} = \begin{bmatrix} \varepsilon_x^0 \\ \varepsilon_y^0 \\ \gamma_{xy}^0 \end{bmatrix} = \begin{bmatrix} \dfrac{\partial U}{\partial x} \\ \dfrac{\partial V}{\partial y} \\ \dfrac{\partial U}{\partial x} + \dfrac{\partial V}{\partial y} \end{bmatrix}, \quad \{\boldsymbol{\kappa}\} = \begin{bmatrix} \kappa_x \\ \kappa_y \\ \kappa_{xy} \end{bmatrix} = \begin{bmatrix} -\dfrac{\partial^2 W}{\partial x^2} \\ -\dfrac{\partial^2 W}{\partial y^2} \\ -2\dfrac{\partial^2 W}{\partial x \partial y} \end{bmatrix}, \tag{3, 4}$$

$$\{\boldsymbol{\lambda}^0\} = \begin{bmatrix} \lambda_x^0 \\ \lambda_y^0 \\ \lambda_{xy}^0 \end{bmatrix} = \begin{bmatrix} \dfrac{1}{2}\left(\dfrac{\partial W}{\partial x}\right)^2 \\ \dfrac{1}{2}\left(\dfrac{\partial W}{\partial y}\right)^2 \\ \dfrac{\partial W}{\partial x}\dfrac{\partial W}{\partial y} \end{bmatrix} \tag{5}$$

U, V and W are displacements of the plate mid-plane.

Coefficients $Q_{ij}^{(k)}$ being the stiffness matrix elements, the stress–strain relation in the kth layer is

$$\begin{Bmatrix} \sigma_x \\ \sigma_y \\ \sigma_{xy} \end{Bmatrix}^{(k)} = \begin{bmatrix} Q_{11} & Q_{12} & Q_{16} \\ Q_{21} & Q_{22} & Q_{26} \\ Q_{61} & Q_{62} & Q_{66} \end{bmatrix}^{(k)} \begin{Bmatrix} \varepsilon_x \\ \varepsilon_y \\ \varepsilon_{xy} \end{Bmatrix}. \tag{6}$$

Denoting by h_k the distance from the middle plane to the upper plane of the kth layer as indicated in Figure 8, the resultant moments and forces are defined as

$$\begin{Bmatrix} M_x \\ M_y \\ M_{xy} \end{Bmatrix} = \sum_{k=1}^{N} \int_{h_{k-1}}^{h_k} \begin{Bmatrix} \sigma_x \\ \sigma_y \\ \sigma_{xy} \end{Bmatrix}^{(k)} z\,\mathrm{d}z, \quad \begin{Bmatrix} N_x \\ N_y \\ N_{xy} \end{Bmatrix} = \sum_{k=1}^{N} \int_{h_{k-1}}^{h_k} \begin{Bmatrix} \sigma_x \\ \sigma_y \\ \sigma_{xy} \end{Bmatrix}^{(k)} \mathrm{d}z. \tag{7, 8}$$

The in-plane forces and bending moments in the plate are given by

$$\begin{bmatrix} \mathbf{N} \\ \mathbf{M} \end{bmatrix} = \begin{bmatrix} \mathbf{A} & \mathbf{B} \\ \mathbf{B} & \mathbf{D} \end{bmatrix} \begin{bmatrix} \{\boldsymbol{\varepsilon}^0\} + \{\boldsymbol{\lambda}^0\} \\ \{\boldsymbol{\kappa}\} \end{bmatrix}, \tag{9}$$

where **A** is the extensional matrix, **B** is the extensional–bending coupling matrix and **D** is the bending matrix of the plate, which are calculated as

$$(A_{ij}, B_{ij}, D_{ij}) = \sum_{k=1}^{N} \int_{h_{k-1}}^{h_k} Q_{ij}^{(k)}\,(1, z, z^2)\,\mathrm{d}z. \tag{10}$$

The expression for the bending strain energy V_b, axial strain energy V_a and the kinetic energy T used in reference [39] have been defined as follows:

$$V_b = \frac{1}{2}\int_S \left\{ D_{11}\left(\frac{\partial^2 W}{\partial x^2}\right)^2 + 2D_{12}\frac{\partial^2 W}{\partial y^2}\frac{\partial^2 W}{\partial x^2} + D_{22}\left(\frac{\partial^2 W}{\partial y^2}\right)^2 \right.$$
$$\left. + 4D_{16}\frac{\partial^2 W}{\partial x^2}\frac{\partial^2 W}{\partial xy} + 4D_{26}\frac{\partial^2 W}{\partial y^2}\frac{\partial^2 W}{\partial xy} + 4D_{66}\left(\frac{\partial^2 W}{\partial xy}\right)^2 \right\} \mathrm{d}S, \tag{11}$$

$$V_a = \frac{1}{2}\int_S \left\{ \frac{A_{11}}{4}\left(\frac{\partial W}{\partial x}\right)^4 + \frac{A_{22}}{4}\left(\frac{\partial W}{\partial y}\right)^4 + \left[\frac{A_{12}}{2} + A_{66}\right]\left(\frac{\partial W}{\partial y}\right)^2\left(\frac{\partial W}{\partial x}\right)^2 + A_{16}\left(\frac{\partial W}{\partial x}\right)^3\frac{\partial W}{\partial y} + A_{26}\left(\frac{\partial W}{\partial y}\right)^3\frac{\partial W}{\partial x} \right\} \mathrm{d}S, \tag{12}$$

$$T = \frac{1}{2}\rho H \int_S \left(\frac{\partial W}{\partial t}\right)^2 \mathrm{d}S, \tag{13}$$

where S is the plate surface $[0, a] \times [0, b]$ and $\mathrm{d}S$ in the elementary surface $\mathrm{d}x\,\mathrm{d}y$.

In the above expressions, the assumption that the in-plane displacements U and V in the energy expressions can be neglected has been made as for the fully clamped rectangular isotropic plates analysis considered in references [30, 35]. The range of validity of this assumption has been extensively discussed in the light of the experimental and numerical results obtained for the frequency amplitude dependence and the bending stress estimates obtained at large vibration amplitudes. The results obtained via this assumption were compared with the previous ones based on various methods such as the finite element method, the method based on Berger's approximation, the ultraspherical polynomial method and the elliptic function method. It was found that the percentage error in the non-linear frequency estimates based on this assumption, for amplitudes up to 1·5 times thickness, does not exceed 1·3% [39]. Also, in the same reference, a comparison between previous results obtained with the present model and results obtained with hierarchical finite element method has shown that the error is 1·01% in the non-linear frequency ratio ω_{nl}/ω_l estimates for amplitudes up to 1 times the plate thickness.

3.2. NUMERICAL MODEL

It is well known that the non-linear response of beams and plates at large vibration amplitudes to harmonic excitation exhibits a harmonic distortion. However, the separation of the higher harmonics carefully carried out at various points of the beam in reference [46], and various points of a plate in reference [30], have shown that the contribution of the higher harmonics to the non-linear response remains small compared with the predominant first harmonic component. Thus, the scope of the present work was restricted mainly to the dependence of the response first harmonic component on the amplitude of vibration and its influence on the associated bending stress patterns. The transverse displacement W of the plate was then approximated using only its first harmonic component as in reference [30], which gives

$$W(x, y, t) = a_k w_k(x, y) \sin \omega t \tag{14}$$

in which the usual summation convention for the repeated index k is used. k is summed over the range 1–n with n being the number of basic functions considered, a_k is the contribution corresponding to the kth basic functions, w_k is the kth basic spatial function.

Discretization of the strain and kinetic energy expressions can be carried out leading to

$$V_h = \tfrac{1}{2}\, a_i a_j k_{ij} \sin^2 \omega t, \quad V_a = \tfrac{1}{2}\, a_i a_j a_k a_l b_{ijkl} \sin^4 \omega t, \quad T = \tfrac{1}{2}\, a_i a_j \omega^2 m_{ij} \cos^2 \omega t \tag{15}$$

in which m_{ij}, k_{ij}, and b_{ijkl} are the mass tensor, the rigidity tensor and the geometrical non-linearity tensor respectively. The expressions for these tensors are

$$k_{ij} = \frac{aH^5E}{b^3} k^*_{ij}, \quad b_{ijkl} = \frac{aH^5E}{b^3} b^*_{ijkl}, \quad m_{ij} = \rho H^3 ab m^*_{ij}, \tag{16–18}$$

where the non-dimensional tensors m^*_{ij}, k^*_{ij} and b^*_{ijkl} are given in terms of integrals of the non-dimensional basic functions w^*_i's, and their first and second partial derivatives (see Appendix A).

Neglecting energy dissipation, the equation of motion derived from Hamilton's principle is

$$\delta \int_0^{2\pi} (V - T)\,\mathrm{d}t = 0. \tag{19}$$

Discretization of the strain and kinetic energy expressions and insertion of these equations in equation (19) using the non-dimensional expressions leads to the following set of non-linear algebraic equations, as shown in Appendix A

$$3a_i a_j a_k b^*_{ijkl} + 2a_i k^*_{ir} - 2a_i \omega^{*^2} m^*_{ir} = 0, \quad i = 1, \ldots, n, \tag{20}$$

which has to be solved numerically.

Details of the discretization procedure, and the expression of the linear parameters m_{ij}, k_{ij} and the non-linear rigidity tensor b_{ijkl} are given in Appendix A.

In order to complete the formulation, as no dissipation is considered here, a supplementary equation is obtained by applying the principle of conservation of energy, which can be written as

$$V_{max} = T_{max}. \tag{21}$$

This leads to the following equation:

$$\omega^{*^2} = \frac{a_i a_j k^*_{ij} + a_i a_j a_k\, a_l b^*_{ijkl}}{a_i a_j m^*_{ij}}, \tag{22}$$

where ω^* is the non-dimensional non-linear frequency parameter.

Substituting equation (22) into equation (21) leads to a system of n non-linear algebraic equations allowing calculation of the contribution coefficients a_i, $i = 1$–n. To obtain the first non-linear mode shape of the plate considered, the contribution of the first basic function is first fixed and the other basic function contributions are calculated via the numerical solutions of the remaining $(n - 1)$ non-linear algebraic equations.

3.3. NUMERICAL RESULTS AND DISCUSSION

3.3.1. *Numerical details*

The problem consists of solving the non-linear algebraic system (20). This system has been solved numerically using the Harwell library routine NS01A. This routine is based on a hybrid iteration method combining the step descent and Newton's method, which do not require a very good initial estimate of the solution [47]. A step procedure, similar to that described in references [29–31, 39] for beams and plates was adopted for ensuring rapid convergence when varying the amplitude, which allowed solutions to be obtained with quite a small number of iterations (an average of 55 iterations for 8 equations).

3.3.2. *Choice of the contributing basic functions and analysis of convergence of the series expansion*

Consider the fully clamped rectangular plate, shown in Figure 3. For such a plate, the deflections in the x and y directions have been represented here by the clamped–clamped beam functions. Beam functions have been used and shown to be appropriate in previous studies of the non-linear vibration of fully clamped rectangular plates [30, 35, 39]. These functions satisfy all the fully clamped theoretical boundary conditions, i.e., zero displacement and zero slope along the four clamped edges. In this paper, the index i used in the series expansion of the plate deflection function W, i.e., equation (14), is replaced by a double index ij:

$$w_k(x, y) = w_{ij}(x, y) \tag{23}$$

in which w_{ij} is the product of the ith and jth clamped–clamped beam functions. The analytical expressions and the shapes of the clamped–clamped beam functions are given in reference [30]. In previous studies, dealing with the first and second non-linear mode shape of fully clamped isotropic plates [30, 35] and the first non-linear mode of rectangular composite plates [39], it was found in each case that the functions which contribute significantly to a given non-linear mode shape are those which contribute significantly to the corresponding linear mode, i.e., nine symmetric–symmetric functions for the first non-linear mode shape of an isotropic plate, nine antisymmetric–symmetric functions for the second mode of an isotropic plate, and 18 basic functions for the first non-linear mode of a CFRP composite plate having a lay-up $(0/\pm 45/90)_{sym}$ due to the non-symmetry induced by the fibre orientation. To start the present work, a procedure based on this conclusion was adopted. So, before considering the non-linear case, a linear analysis was made using 36 basic functions in order to determine the basic functions which have to be used in the non-linear case. It had led to the conclusion that only nine functions needs to be taken into account. This has been attributed to the fact that although the plate considered is a composite plate, it has a particular cross-ply lay-up, which leads to $D_{16} = D_{26} = 0$. Then, to confirm the validity of this conclusion, calculations have been made in the non-linear case using 25 basic functions in order to check that the omitted functions have negligible contributions, as discussed below.

TABLE 4

First linear mode shape of a fully clamped Glare 3 *hybrid composite panel* ($\alpha = 0{\cdot}6$): *typical numerical results obtained with* 36 *basic functions*

	ω_l^*	7·583			
1	a_{11}	1	19	a_{41}	– 3·9509E – 11
2	a_{12}	– 1·3684E – 10	20	a_{42}	– 3·3979E – 18
3	a_{13}	5·2839E – 03	21	a_{43}	2·0876E – 12
4	a_{14}	– 4·7107E – 12	22	a_{44}	8·6467E – 19
5	a_{15}	6·9653E – 04	23	a_{45}	5·1182E – 13
6	a_{16}	5·5464E – 11	24	a_{46}	– 1·1737E – 20
7	a_{21}	– 7·0045E – 10	25	a_{51}	5·0492E – 03
8	a_{22}	2·3285E – 18	26	a_{52}	1·3355E – 12
9	a_{23}	– 7·3278E – 12	27	a_{53}	– 1·1269E – 03
10	a_{24}	3·3996E – 19	28	a_{54}	5·0116E – 13
11	a_{25}	– 1·0479E – 12	29	a_{55}	– 2·8726E – 04
12	a_{26}	– 2·9915E – 20	30	a_{56}	– 4·1164E – 13
13	a_{31}	3·1892E – 02	31	a_{61}	6·6546E – 11
14	a_{32}	9·7385E – 13	32	a_{62}	– 1·8522E – 19
15	a_{33}	– 1·9421E – 03	33	a_{63}	– 7·8555E – 13
16	a_{34}	6·8114E – 13	34	a_{64}	8·2710E – 20
17	a_{35}	– 3·5816E – 04	35	a_{65}	– 9·1700E – 14
18	a_{36}	6·7363E – 13	36	a_{66}	2·9994E – 21

3.3.3. *Results of linear analysis of fully clamped G3HCRP vibrations*

Table 4 summarizes the results of linear analysis obtained for a plate having an aspect ratio $\alpha = 0{\cdot}6$. It appears clearly in this table that only nine functions obtained as products of the three first symmetric beam functions in both x and y direction contribute significantly to the first mode shape of the fully clamped G3HCRP. The ratio of the highest contribution of the omitted functions to the smallest contribution of the significant functions (a_{12}/a_{35}) is about $3{\cdot}82 \times 10^{-7}$.

3.3.4. *Typical non-linear results obtained with* 25 *functions*

To check the validity of the conclusion reached in section 3.3.3, according to which nine functions are sufficient to obtain a good estimate of the fundamental non-linear mode shape, typical calculations have been made using 25 basic functions obtained as products of the first five clamped–clamped beam mode shapes, which has led to the solution of 24 non-linear algebraic equations.

Typical values of the a_{ij}'s obtained are given in Table 5 for different values of w^*_{max}. It can be seen that the only significant contributions, as may be expected due to the symmetry of the plate's first non-linear mode shape, are those corresponding to the first nine symmetric basic functions in both the x and y directions. To check that the addition of the

TABLE 5

First non-linear mode shape of a fully clamped G3HCRP ($\alpha = 0{\cdot}6$): *typical numerical results obtained with* 25 *basic functions* (*obtained as product of the first five clamped–clamped beam functions*)

	w^*_{max}	0·0228	0·7665	2·7749
	ω^*_{nl}/ω^*_l	1·000076	1·079	1·6404
1	a_{11}	0·009	0·3	1·05
2	a_{12}	−2·0648E−12	−5·6230E−11	−3·7560E−10
3	a_{13}	4·7615E−05	3·4600E−03	3·7671E−02
4	a_{14}	−7·7319E−13	−4·1184E−12	−6·0689E−11
5	a_{15}	6·2942E−06	1·0683E−03	2·1258E−02
6	a_{21}	8·1996E−11	−2·0773E−10	−6·8508E−10
7	a_{22}	1·4787E−11	−7·4143E−17	2·8568E−19
8	a_{23}	1·9859E−12	−3·7249E−12	−3·2702E−11
9	a_{24}	−4·2381E−13	−1·4456E−17	5·9813E−20
10	a_{25}	−1·3493E−13	−1·0177E−12	−1·5957E−11
11	a_{31}	2·8725E−04	1·6143E−02	1·2903E−01
12	a_{32}	−8·3692E−13	−1·7113E−12	−5·2579E−11
13	a_{33}	−1·7466E−05	−6·9134E−05	1·3673E−02
14	a_{34}	−1·7496E−13	9·0084E−13	3·8424E−12
15	a_{35}	−3·2299E−06	−2·9644E−04	−2·0251E−03
16	a_{41}	4·7325E−12	−1·6268E−11	−9·6766E−11
17	a_{42}	1·1360E−13	−4·6643E−17	5·1851E−20
18	a_{43}	6·8989E−13	1·2335E−13	−1·0188E−11
19	a_{44}	1·8332E−14	7·5834E−18	9·7924E−21
20	a_{45}	−1·7084E−13	1·7691E−13	−1·4390E−12
21	a_{51}	4·5461E−05	2·2197E−03	2·5186E−02
22	a_{52}	4·8163E−13	2·2870E−13	−1·0560E−11
23	a_{53}	−1·0145E−05	−3·7457E−04	2·4329E−03
24	a_{54}	−8·5231E−13	1·2998E−13	8·0932E−13
25	a_{55}	−2·5845E−06	−7·2546E−05	−3·5977E−04

TABLE 6

First non-linear mode shape of a fully clamped G3HCRP ($\alpha = 0{\cdot}6$): *typical numerical results obtained with* 9 *well-chosen basic functions*

	w^*_{max} ω^*_{nl}/ω^*_l	0·0220 1·000076	0·7213 1·079	2·4059 1·6404
1	a_{11}	0·009	0·3	1·05
2	a_{13}	4·7615E−05	3·4600E−03	3·7671E−02
3	a_{15}	6·2942E−06	1·0683E−03	2·1258E−02
4	a_{31}	2·8725E−04	1·6143E−02	1·2903E−01
5	a_{33}	−1·7466E−05	−6·9134E−05	1·3673E−02
6	a_{35}	−3·2299E−06	−2·9644E−04	−2·0251E−03
7	a_{51}	4·5461E−05	2·2197E−03	2·5186E−02
8	a_{53}	−1·0145E−05	−3·7457E−04	2·4329E−03
9	a_{55}	−2·5845E−06	−7·2546E−05	−3·5977E−04

TABLE 7

Comparison of contribution coefficients to the first mode shape of a fully clamped G3HCRP for $\alpha = 0{\cdot}2$, $\alpha = 0{\cdot}6$ *and* $\alpha = 0{\cdot}8$; (*a*) *linear results calculated here* (*b*) *present results obtained from non-linear analysis*

	$\alpha = 0{\cdot}2$ and $w^*_{max} = 0{\cdot}0263$		$\alpha = 0{\cdot}6$ and $w^*_{max} = 0{\cdot}0245$		$\alpha = 0{\cdot}8$ and $w^*_{max} = 0{\cdot}0246$	
	(a)	(b)	(a)	(b)	(a)	(b)
ω^*_l	6·648	6·649	7·583	7·584	8·745	8·746
a_{11}	1	1	1	1	1	1
a_{13}	0·00058758	0·00059474	0·00528385	0·00529212	0·00910448	0·00911414
a_{15}	0·00007370	0·00007721	0·00069653	0·00070002	0·00123451	0·00123789
a_{31}	0·09237948	0·09281924	0·03189222	0·03192192	0·02017104	0·02018732
a_{33}	−0·00005858	−0·00005773	−0·00194215	−0·00194028	−0·00276109	−0·00275858
a_{35}	−0·00000775	−0·00000831	−0·00035816	−0·00035905	−0·00064874	−0·00064957
a_{51}	0·02435734	0·02438565	0·00504923	0·00505173	0·00293743	0·00294032
a_{53}	−0·00015673	−0·00015675	−0·00112691	−0·00112726	−0·00109317	−0·00109371
a_{55}	−0·00002207	−0·00002205	−0·00028726	−0·00028715	−0·00037648	−0·00037636

antisymmetric functions does not affect the results, calculations have been made with only nine symmetric functions in both the x and y directions. The results presented in Table 6 show no significant change in both the value of the resonance frequencies and the basic function contributions. This confirmed the conclusion that good estimates of the non-linear mode shapes can be obtained by solving only eight equations corresponding to nine well-chosen basic functions.

3.3.5. *Comparison of results obtained from the non-linear model at small amplitudes with linear results*

In previous works [29–32, 35, 37–39], the model has been validated both numerically and experimentally. In this section, in order to validate the theory and the numerical results obtained in the present work, comparison is made between results obtained here from the non-linear model when the amplitudes of vibrations considered are very small and data obtained from the linear analysis. Table 7 shows a comparison of numerical results obtained from the solution of the set of non-linear algebraic equations (20), corresponding to the non-linear problem, obtained for small vibration amplitudes, with those based on the linear analysis. It can be seen that the resonance frequencies and the contributions of the basic functions obtained via both analyses are very close.

3.3.6. *General presentation of numerical results*

Numerical results for a fully clamped G3HCRP corresponding to assigned values of a_{11} varying from 0·05 to 1·05, which correspond to maximum displacement amplitude to thickness ratios varying from 0·1233 to 2·5184, obtained at $(x^*, y^*) = (0{\cdot}5, 0{\cdot}5)$, and $\alpha = 0{\cdot}2$, 0·6 and 1, are summarized in Tables 8–10. In each Table, a_{ij} represents the contribution of the basic function obtained as product of the ith and the jth x and y clamped–clamped beam functions. w^*_{max} is the maximum non-dimensional amplitude obtained at the plate centre and ω^*_{nl}/ω^*_l is the ratio of the non-linear non-dimensional frequency parameter defined in equation (22) to the linear non-dimensional frequency parameter obtained by solution of the linear eigenvalue problem. It can be seen that in the non-linear numerical results corresponding to the square plate ($\alpha = 1$), the contribution coefficients a_{ij} are, as may be expected due to the quasi-complete symmetry of the problem in this case, almost identical to a_{ji} (for $i = 1$, 2, 3 and $j = 1$, 2, 3) for all values of vibration amplitudes. This may be considered as an additional check of the good convergence of the iterative method used for solving the set of non-linear algebraic equations.

3.3.7. *Amplitude dependence of the fundamental mode shape and comparison with experimental results*

Comparison with experimental measurements is the best way to verify numerical results. The model has been validated in previous published works [29–31, 35, 39]. In this section, a comparison between numerical and experimental results has been made. Measurements were carried out on a G3HCRP described in section 2.2.1. The plate was harmonically excited by a coil and magnet exciter in the region of its first resonance determined by frequency response tests. For the first non-linear mode shape measurements, the excitation point was chosen to be at the middle of the plate. The electrodynamic exciter imposed no added stiffness and little additional mass on the structure. In order not to load the plate with a response measurement transducer, a non-contacting Laster Velocity-Transducer set type 3544 was used for measuring the non-linear dynamic response along sections across the plate area. The output from the laser velocity-transducer is a voltage–time signal proportional to either the velocity or displacement of the target surface. The experimental measurements are presented in this section and compared to numerical results. Figures 9(a) and (b) show the measured normalized separated first harmonic component along the x and y direction for a maximum non-dimensional amplitude w^*_{max} of 0·35 together with the normalized theoretical non-linear mode shape. As may be expected, due to the rigidity introduced in the theory by the truncation of the series in the spectral expansion of the displacement function, the theoretical curve is higher than the experimental values in the intermediate regions of the normalized curves but it can be seen that the non-linear prediction and measured values are close. The non-linear experimental values and theoretical curve do not coincide exactly, due to various experimental errors and theoretical approximations. It can be seen, however, that the trends of deformation of the non-linear mode shapes are very similar.

The good qualitative agreement between the non-dimensional first non-linear mode shape calculated from the theoretical model and experimental measurements of a fully clamped G3HCRP, confirms the conclusion reached in reference [39], according to which

TABLE 8

Contribution coefficients to the first non-linear mode shape of fully clamped G3HCRP, $\alpha = 0{\cdot}2$

w^*_{max}	ω^*_{nl}/ω^*_l	a_{11}	a_{13}	a_{15}	a_{31}	a_{33}	a_{35}	a_{51}	a_{53}	a_{55}
0·1174	1·0024	0·05	3·8212E−05	8·0169E−06	5·1448E−03	−1·8274E−06	−1·0156E−06	1·2564E−03	−7·8390E−06	−1·1083E−06
0·2295	1·0093	0·10	1·2716E−04	4·1131E−05	1·2937E−02	3·7403E−06	−4·3943E−06	2·8029E−03	−1·5130E−05	−2·7605E−06
0·3352	1·0202	0·15	3·0980E−04	1·2149E−04	2·4243E−02	2·6517E−05	−7·7087E−06	5·0622E−03	−1·9093E−05	−6·7063E−06
0·4369	1·0348	0·20	6·2122E−04	2·6860E−04	3·8381E−02	7·7542E−05	−4·7281E−06	8·3733E−03	−1·4419E−05	−1·4163E−05
0·5371	1·0528	0·25	1·0895E−03	5·0015E−04	5·4251E−02	1·6689E−04	1·1314E−05	1·2803E−02	5·3830E−06	−2·4256E−05
0·6374	1·0740	0·30	1·7347E−03	8·3166E−04	7·0986E−02	3·0269E−04	4·6033E−05	1·8197E−02	4·6490E−05	−3·4428E−05
0·7384	1·0980	0·35	2·5686E−03	1·2761E−03	8·8060E−02	4·9093E−04	1·0372E−04	2·4316E−02	1·1389E−04	−4·1571E−05
0·8402	1·1246	0·40	3·5945E−03	1·8435E−03	1·0520E−01	7·3567E−04	1·8767E−04	3·0931E−02	2·1110E−04	−4·2807E−05
0·9427	1·1535	0·45	4·8091E−03	2·5410E−03	1·2226E−01	1·0392E−03	3·0044E−04	3·7862E−02	3·4029E−04	−3·5805E−05
1·0459	1·1846	0·50	6·2033E−03	3·3730E−03	1·3921E−01	1·4021E−03	4·4407E−04	4·4978E−02	5·0243E−04	−1·8800E−05
1·1495	1·2175	0·55	7·7645E−03	4·3414E−03	1·5603E−01	1·8239E−03	6·2014E−04	5·2192E−02	6·9758E−04	9·4853E−06
1·3577	1·2880	0·65	1·1327E−02	6·6844E−03	1·8930E−01	2·8357E−03	1·0740E−03	6·6715E−02	1·1838E−03	1·0317E−04
1·5667	1·3638	0·75	1·5367E−02	9·5469E−03	2·2218E−01	4·0510E−03	1·6669E−03	8·1193E−02	1·7882E−03	2·4923E−04
1·7764	1·4438	0·85	1·9764E−02	1·2887E−02	2·5478E−01	5·4391E−03	2·3989E−03	9·5550E−02	2·4959E−03	4·4873E−04
1·9865	1·5271	0·95	2·4415E−02	1·6651E−02	2·8719E−01	6·9676E−03	3·2653E−03	1·0977E−01	3·2902E−03	7·0094E−04
2·1969	1·6131	1·05	2·9241E−02	2·0783E−02	3·1946E−01	8·6059E−03	4·2581E−03	1·2387E−01	4·1549E−03	1·0039E−03

TABLE 9

Contribution coefficients to the first non-linear mode shape of a fully clamped G3HCRP, $\alpha = 0{\cdot}6$

w^*_{max}	ω^*_{nl}/ω^*_l	a_{11}	a_{13}	a_{15}	a_{31}	a_{33}	a_{35}	a_{51}	a_{53}	a_{55}
0·1225	1·0024	0·05	2·7445E−04	3·9183E−05	1·6319E−03	−9·4771E−05	−1·9009E−05	2·5560E−04	−5·6744E−05	−1·4232E−05
0·2444	1·0095	0·10	6·0914E−04	1·0421E−04	3·4818E−03	−1·7545E−04	−4·4440E−05	5·3021E−04	−1·1568E−04	−2·7741E−05
0·3655	1·0210	0·15	1·0581E−03	2·1950E−04	5·7407E−03	−2·2771E−04	−8·1829E−05	8·4356E−04	−1·7810E−04	−4·0092E−05
0·4855	1·0367	0·20	1·6648E−03	4·0689E−04	8·5529E−03	−2·3695E−04	−1·3517E−04	1·2162E−03	−2·4376E−04	−5·1305E−05
0·6041	1·0562	0·25	2·4595E−03	6·8487E−04	1·2008E−02	−1·8867E−04	−2·0659E−04	1·6685E−03	−3·1054E−04	−6·1857E−05
0·7213	1·0791	0·30	3·4600E−03	1·0683E + 05	1·6143E−02	−6·9134E−05	−2·9644E−04	2·2197E−03	−3·7457E−04	−7·2546E−05
0·8373	1·1049	0·35	4·6730E−03	1·5683E−03	2·0953E−02	1·3401E−04	−4·0347E−04	2·8863E−03	−4·3057E−04	−8·4279E−05
0·9522	1·1334	0·40	6·0964E−03	2·1928E−03	2·6400E−02	4·3112E−04	−5·2533E−04	3·6806E−03	−4·7235E−04	−9·7873E−05
1·0660	1·1642	0·45	7·7217E−03	2·9465E−03	3·2430E−02	8·3019E−04	−6·5888E−04	4·6110E−03	−4·9341E−04	−1·1390E−04
1·1791	1·1969	0·50	9·5365E−03	3·8315E−03	3·8975E−02	1·3367E−03	−8·0061E−04	5·6813E−03	−4·8734E−04	−1·3263E−04
1.2915	1·2315	0·55	1·1526E−02	4·8476E−03	4·5968E−02	1·9538E−03	−9·4688E−04	6·8913E−03	−4·4825E−04	−1·5396E−04
1·5152	1·3051	0·65	1·5961E−02	7·2636E−03	6·1040E−02	3·5209E−03	−1·2391E−03	9·7149E−03	−2·5150E−04	−2·0273E−04
1·7379	1·3051	0·75	2·0901E−02	1·0162E−02	7·7185E−02	5·5167E−03	−1·5102E−03	1·3029E−02	1·2650E−04	−2·5471E−04
1.9604	1.4661	0·85	2·6227E−02	1·3497E−02	9·4053E−02	7·9058E−03	−1·7403E−03	1·6762E−02	7·0040E−04	−3·0275E−04
2·1830	1·5519	0·95	3·1843E−02	1·7214E−02	1·1139E−01	1·0641E−02	−1·9150E−03	2·0838E−02	1·4719E−03	−3·3975E−04
2·4059	1.6404	1·05	3·7671E−02	2·1258E−02	1·2903E−01	1·3673E−02	−2·0251E−03	2·5186E−02	2·4329E−03	−3·5977E−04

Table 10

Contribution coefficients to the first non-linear mode shape of a fully clamped G3HCRP, $\alpha = 1$

w^*_{max}	ω^*_{nl}/ω^*_l	a_{11}	a_{13}	a_{15}	a_{31}	a_{33}	a_{35}	a_{51}	a_{53}	a_{55}
0·1233	1·0023	0·05	6·9880E−04	9·9457E−05	6·9880E−04	−1·4690E−04	−4·5938E−05	9·9457E−05	−4·5938E−05	−1·9938E−05
0·2464	1·0093	0·10	1·4846E−03	2·2232E−04	1·4846E−03	−2·7291E−04	−9·7061E−05	2·2232E−04	−9·7061E−05	−3·8954E−05
0·3690	1·0206	0·15	2·4359E−03	3·9099E−04	2·4359E−03	−3·5744E−04	−1·5792E−04	3·9099E−04	−1·5792E−04	−5·6237E−05
0·4911	1·0361	0·20	3·6162E−03	6·2588E−04	3·6162E−03	−3·8062E−04	−2·3193E−04	6·2588E−04	−2·3193E−04	−7·1144E−05
0·6126	1·0554	0·25	5·0704E−03	9·4475E−04	5·0704E−03	−3·2377E−04	−3·2108E−04	9·4475E−04	−3·2108E−04	−8·3207E−05
0·7335	1·0781	0·30	6·8246E−03	1·3622E−03	6·8246E−03	−1·7003E−04	−4·2586E−04	1·3622E−03	−4·2586E−04	−9·2066E−05
0·8537	1·1038	0·35	8·8878E−03	1·8895E−03	8·8878E−03	9·5158E−05	−5·4541E−04	1·8895E−03	−5·4541E−04	−9·7382E−05
0·9735	1·1323	0·40	1·1256E−02	2·5344E−03	1·1256E−02	4·8363E−04	−6·7774E−04	2·5344E−03	−6·7774E−04	−9·8746E−05
1·0928	1·1631	0·45	1·3914E−02	3·3017E−03	1·3914E−02	1·0043E−03	−8·2004E−04	3·3017E−03	−8·2004E−04	−9·5609E−05
1·2117	1·1959	0·50	1·6842E−02	4·1932E−03	1·6842E−02	1·6630E−03	−9·6899E−04	4·1932E−03	−9·6899E−04	−8·7255E−05
1·3304	1·2306	0·55	2·0016E−02	5·2085E−03	2·0016E−02	2·4630E−03	−1·1210E−03	5·2085E−03	−1·1210E−03	−7·2795E−05
1·5675	1·3046	0·65	2·7000E−02	7·5987E−03	2·7000E−02	4·4869E−03	−1·4198E−03	7·5987E−03	−1·4198E−03	−2·1347E−05
1·8045	1·3836	0·75	3·4671E−02	1·0436E−02	3·4671E−02	7·0568E−03	−1·6896E−03	1·0436E−02	−1·6896E−03	6·7841E−05
2·0419	1·4667	0·85	4·2862E−02	1·3669E−02	4·2862E−02	1·0130E−02	−1·9079E−03	1·3669E−02	− 1·9079E−03	2·0386E−04
2·2798	1·5531	0·95	5·1437E−02	1·7244E−02	5·1437E−02	1·3652E−02	−2·0586E−03	1·7244E−02	−2·0586E−03	3·9451E−04
2·5184	1·6423	1·05	6·0292E−02	2·1104E−02	6·0292E−02	1·7561E−02	−2·1309E−03	2·1104E−02	−2·1309E−03	6·4552E−04

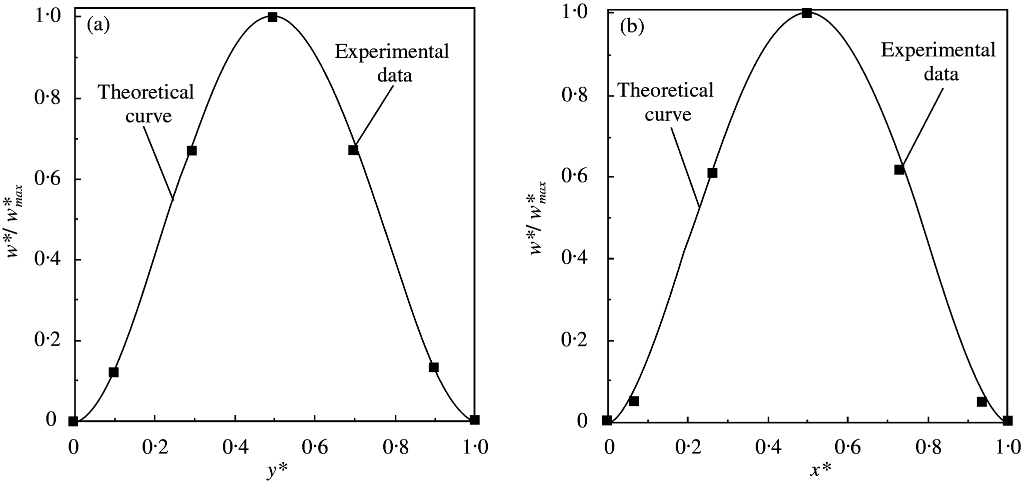

Figure 9. Comparison of the normalized first harmonic component along the section (a) $x^* = 0{\cdot}5$ and $\alpha = \frac{2}{3}$ G3HCRP. $w^*_{max} = 0{\cdot}35$; (b) $y^* = 0{\cdot}5$ and $\alpha = \frac{2}{3}$ G3HCRP. $w^*_{max} = 0{\cdot}35$.

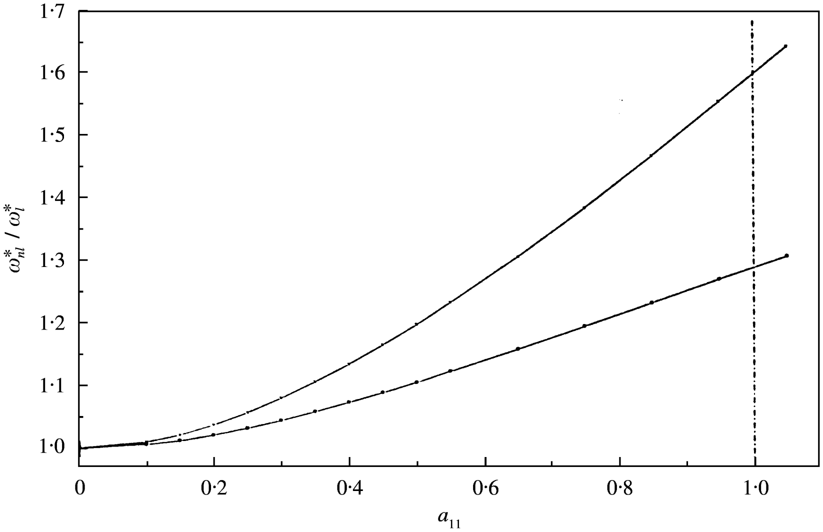

Figure 10. Comparison of the change in natural frequency at large amplitudes for G3HCP and isotropic plates $\alpha = 0{\cdot}6$. —●— isotropic plate studied in reference [34]; —·— Glare 3 panel.

the theoretical model based on Hamilton's principle and spectral analysis can be a good tool for analyzing geometrically non-linear free vibration problems of composites. The dependence of the non-linear frequency on the amplitude of vibration is plotted in Figure 10, for both the first mode of a fully clamped isotropic rectangular plate and a fully clamped G3HCRP ($\alpha = 0{\cdot}6$), with the ratio of non-dimensional non-linear frequency to the linear frequency ω^*_{nl}/ω^*_l against the vibration amplitude coefficient a_{11}. The curves of this figure show that the first non-linear mode of fully clamped G3HCRP exhibits a greater change in frequency with amplitude than does the first non-linear mode of an isotropic plate of the same thickness. It can be seen that for $a_{11} = 1$, which corresponds to

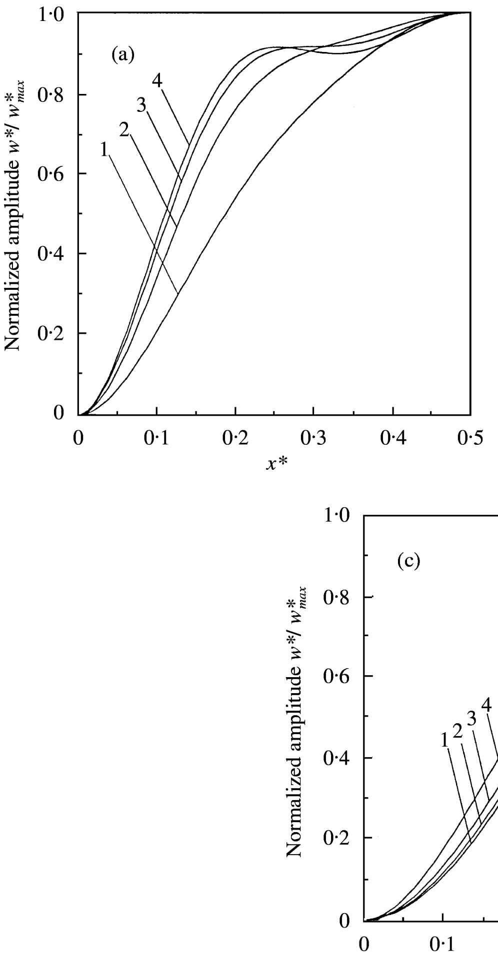

Figure 11. (a) Normalized amplitude first non-linear rectangular G3HCRP, $\alpha = 0{\cdot}2$, $y^* = 0{\cdot}5$: (curve 1) lowest amplitude; (curve 4) highest amplitude. (b) Normalized amplitude first non-linear rectangular G3HCRP, $\alpha = 0{\cdot}6$, $y^* = 0{\cdot}5$: (curve 1) lowest amplitude; (curve 4) highest amplitude. (c) Normalized amplitude first non-linear square G3HCRP, $\alpha = 1$, $y^* = 0{\cdot}5$: (curve 1) lowest amplitude; (curve 4) highest amplitude.

a non-dimensional amplitude at the plate centre equal to $1{\cdot}5 \times 1{\cdot}5 \times 1 = 2{\cdot}25$ approximately, the increase of non-linear natural frequency for the isotropic plate is somewhat above 28% while the corresponding increase for the G3HCRP is about 60%. Figures 11(a)–(c) show the normalized fundamental mode shape for various aspect ratios $\alpha = 0{\cdot}2$, $0{\cdot}6$ and 1, respectively, of G3HCRP along the middle line ($y^* = 0{\cdot}5$) for different amplitudes. The mode shapes are normalized by division by the maximum value, obtained at the centre of the plate. The four lines represent the mode shapes corresponding to $a_{11} = 0{\cdot}05$, $0{\cdot}3$, $0{\cdot}55$ and $1{\cdot}05$ which correspond to the maximum non-dimensional amplitudes given in Table 11. It can be seen that the curvature near the edge increases gradually with increase of the amplitude. Similar curves corresponding to $y^* = 0{\cdot}025$ and $\alpha = 0{\cdot}2$, $0{\cdot}6$ and 1 along the x^* normalized section are presented in Figures 12(a)–(c). It was generally noticed that the deformation of the mode shape, for a given value of the normalized amplitude of vibration, increases as the aspect ratio α decreases. Also, it appears

Table 11

Maximum displacement amplitude w^*_{max} *corresponding to the normalized curves given in Figures* 11, 12, 14 *and* 15

	Aspect ratio α	0·2	0·6	1
w^*_{max}	Curve 1	0·1174	0·1225	0·1233
	Curve 2	0·6374	0·7213	0·7335
	Curve 3	1·1495	1·2915	1·3304
	Curve 4	2·1969	2·4059	2·5184

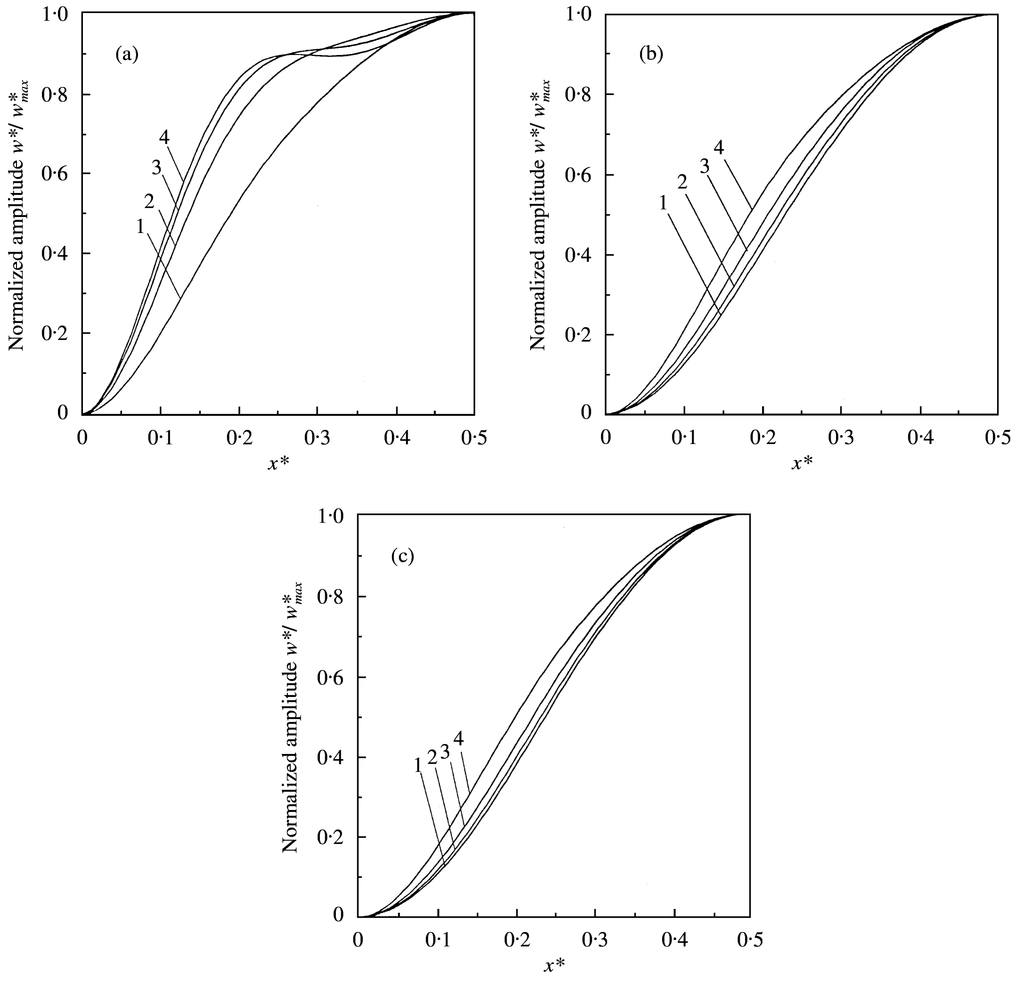

Figure 12. (a) Normalized amplitude first non-linear rectangular G3HCRP, $\alpha = 0·2$, $y^* = 0·025$: (curve 1) lowest amplitude; (curve 4) highest amplitude. (b) Normalized amplitude first non-linear rectangular G3HCRP, $\alpha = 0·6$, $y^* = 0·025$: (curve 1) lowest amplitude; (curve 4) highest amplitude. (c) Normalized amplitude first non-linear square G3HCRP, $\alpha = 1$, $y^* = 0·025$: (curve 1) lowest amplitude; (curve 4) highest amplitude.

clearly that the non-linear mode shape in the neighbourhood of the clamps can be very different from that usually expected in linear theory.

3.3.8. *Bending stresses associated with the first non-linear mode shape*

Using the stress–strain relationship (6), the maximum bending stress σ_{xb} and σ_{yb} obtained for $z = H/2$ are given by

$$\sigma_{xb} = \frac{H}{2} Q_{11} \frac{\partial^2 W}{\partial x^2} + \frac{H}{2} Q_{12} \frac{\partial^2 W}{\partial y^2}, \quad \sigma_{yb} = \frac{H}{2} Q_{12} \frac{\partial^2 W}{\partial x^2} + \frac{H}{2} Q_{22} \frac{\partial^2 W}{\partial y^2}. \quad (24, 25)$$

In terms of the non-dimensional parameters defined in the previous work [11], non-dimensional stresses σ^*_{xb} and σ^*_{yb} can be defined by

$$\sigma^*_{xb} = \alpha^2 \frac{\partial^2 W^*}{\partial x^{*^2}} + v \frac{\partial^2 W^*}{\partial y^{*^2}}, \quad \sigma^*_{yb} = v\alpha^2 \frac{\partial^2 W^*}{\partial x^{*^2}} + \frac{\partial^2 W^*}{\partial y^{*^2}} \quad (26, 27)$$

with $\alpha = b/a$. The relationship between the dimensional and non-dimensional stresses is

$$\sigma = \frac{EH^2}{2(1 - v^2)\, b^2} \sigma^*, \quad (28)$$

which is valid for both dimensional and non-dimensional pairs of stresses defined by equations (24)–(27).

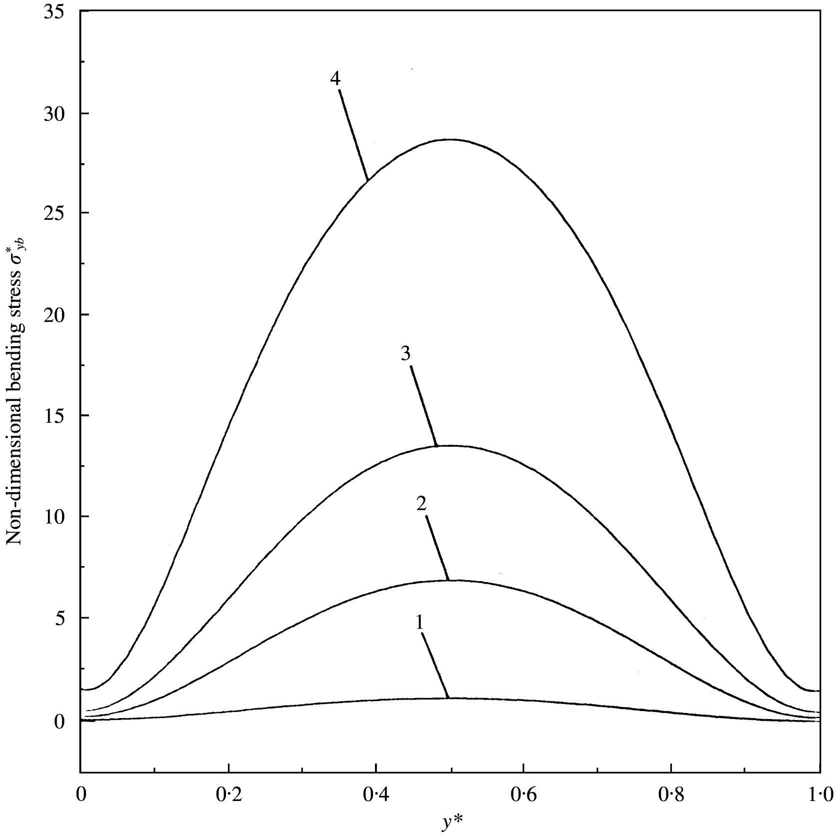

Figure 13. Non-dimensional bending stress distribution associated with the fully clamped square G3HCRP first non-linear mode for $\alpha = 1$ along the section $x^* = 0{\cdot}025$: (curve 1) lowest; (curve 2) highest.

The non-dimensional bending stress distribution for G3HCRP is plotted in Figures 13, 14(a), (b), 15(a) and (b). As was found in references [30, 39], it can be seen in Figure 13 that the bending stress distribution can exhibit in the neighbourhood of the clamps a distribution with positive values along the whole section, due to the Poisson ratio effect and due to high curvatures in the y direction. In Figures 14(a), (b), 15(a) and (b) the non-dimensional bending stress distribution is plotted for various plate aspect ratios and various sections of the mode. All curves show the amplitude dependence of the stress

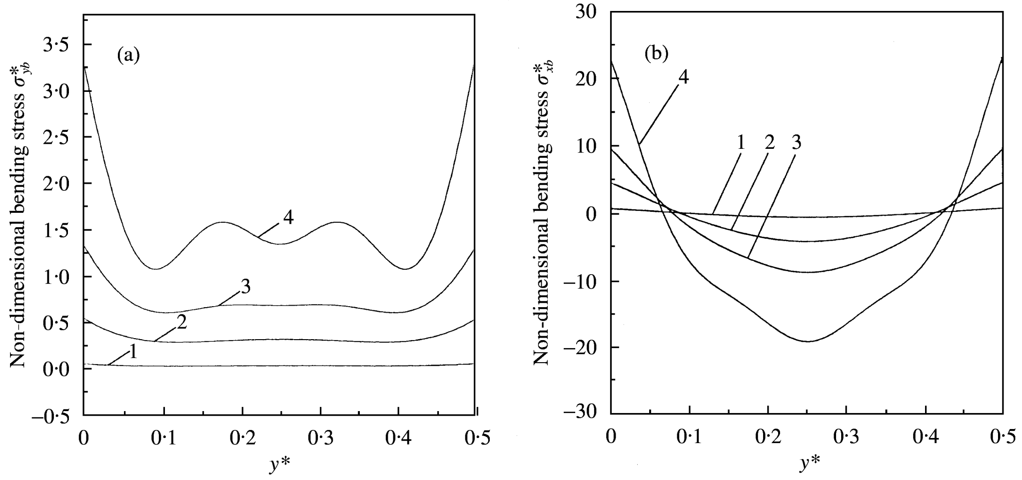

Figure 14. (a) Non-dimensional bending stress distribution associated with the fully clamped rectangular G3HCRP first non-linear mode for $\alpha = 0{\cdot}2$ along the section $x^* = 0{\cdot}025$: (curve 1) lowest; (curve 4) highest. (b) Non-dimensional bending stress distribution associated with the fully clamped rectangular G3HCRP first non-linear mode for $\alpha = 0{\cdot}6$ along the section $x^* = 0{\cdot}025$: (curve 1) lowest amplitude; (curve 4) highest amplitude.

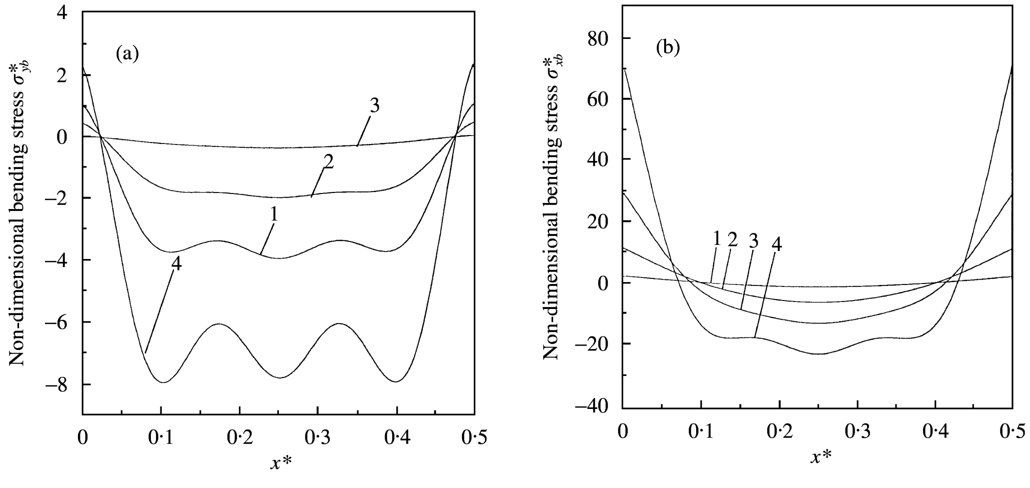

Figure 15. (a) Non-dimensional bending stress distribution associated with the fully clamped rectangular G3HCP first non-linear mode for $\alpha = 0{\cdot}2$ along the section $y^* = 0{\cdot}25$: (curve 1) lowest amplitude; (curve 4) highest amplitude. (b) Non-dimensional bending stress distribution associated with the fully clamped rectangular G3HCRP first non-linear mode for $\alpha = 1$ along the section $y^* = 0{\cdot}25$: (curve 1) lowest amplitude; (curve 4) highest amplitude.

TABLE 12

Comparison of the rate of increase of the non-dimensional bending stress σ^*_{xh} *with increasing* w^*_{max} *at various points*: $A(x^*, y^*) = (0{\cdot}025;\ 0{\cdot}025)$; B: (0·25; 0·025); C: (0·5; 0·025); D: (0·025; 0·25); $R(w^*)$: *rate of increase of* w^*_{max}; $R(\sigma^*_{xb})$: *rate of increase of* σ^*_{xb}. *The reference value is the first value. G3HCRP* $\alpha = 0{\cdot}6$

ω^*_{nl}/ω^*_l	w^*_{max}	$R(w^*)$	$\sigma^*(A)$	$R(\sigma^*(A))$	$\sigma^*(B)$	$R(\sigma^*(B))$	$\sigma^*(C)$	$R(\sigma^*(C))$	$\sigma^*(D)$	$R(\sigma^*(D))$
1·00245	0·1225		0·0201		0·5984		1·0415		0·7185	
1·1969	1·1791	9·6253	0·287	14·2079	7·1057	11·8745	11·2176	10·7706	9·0717	12·6259
1·6404	2·4059	19·64	0·9577	47·6467	18·4912	30·9011	26·3403	25·2907	24·7280	34·4161

distribution, and a high increase of the bending stress near the clamps, compared with the rate of increase expected in linear theory. Table 12 summarizes some numerical data concerning the non-linear increase in bending stress with the amplitude of vibration. Considering a G3HCRP corresponding to $\alpha = \frac{2}{3}$, it appears that the non-dimensional bending stress σ^*_{xh} obtained at the point $A(x^* = 0{\cdot}025,\ y^* = 0{\cdot}025)$ of the plate, increases from 0·0201 to 0·9577, when the maximum non-dimensional amplitude w^*_{max} increases from 0·1225 to 2·4059. This shows that the non-linear analysis predicts an increase in σ^*_{xb} which is higher than that expected from a linear analysis.

4. CONCLUSIONS

The main objective of this paper was to investigate both experimentally and numerically the linear and non-linear dynamic response of fully clamped G3HCRP. In the linear study, experimental modal tests have been carried out on a fully clamped G3HCRP. The natural frequencies and mode shapes obtained by the experimental and theoretical predictions were close. The modal damping data were obtained. A typical damping ratio for the G3HCRP is 0·7%. Modal assurance criterion (MAC) data were used and have shown that all of the modal results are satisfactory. Concerning the non-linear results, the geometrically non-linear free vibration analysis (first mode) of G3HCRP has been successfully carried out using the model based on Hamilton's principle and spectral analysis. Good agreement has been found between experimental and numerical results. The study has shown that the fundamental mode shape is amplitude dependent. Also, the non-dimensional bending stress distribution associated with the G3HCRP first non-linear mode for different amplitudes of vibration has been investigated. It was also shown that the bending stress could exhibit in the neighbourhood of the clamps, a distribution with positive values along the whole section. This is due to the Poisson ratio effect and due to high curvatures in the other direction.

Comparison of the changes in non-linear resonant frequency at large vibration amplitudes for isotropic and G3HCRP show an increase of the non-dimensional non-linear frequency parameter with increasing a_{11} for the first mode, which is much greater for the G3HCRP than that obtained for an isotropic plate.

It has also been found that accurate results can be achieved by using the present model with only nine basic functions which was attributed to the particular plate lay-up which leads to $D_{16} = D_{26} = 0$. In a previous work [39] it was shown that for some plates having different fibre orientation, 18 basic functions were necessary to estimate the fundamental CFRP non-linear mode shape. Based on these results, further work is needed to investigate the behaviour of higher modes and the effects of fibre orientations.

ACKNOWLEDGMENTS

The first author would like to thank Dr Y. Xiao and Mr P. R. Cunningham from the department of Aeronautics and Astronautics (University of Southampton) for their helpful discussions and Mr J. R. Baker from the Institute of Sound and Vibration Research for his very useful and much appreciated technical assistance.

REFERENCES

1. D. H. MIDDLESTONE (editor) 1990 *Composite Materials in Aircraft Structures*. Harlow: Longman Scientific & Technical.
2. M. V. LOWSON 1989 *Proceedings of the Royal Aeronautical Society Conference on Aerospace Applications of Advanced Materials, UK*. Future use of advanced materials.
3. Y. XIAO 1997 Progress report, *Institute of Sound and Vibration Research*. Development of design techniques for the avoidance of acoustic fatigue in aircraft box-type structures, Part I: review of composite materials.
4. P. T. ELANGOVAN *et al.* 1994 *Symposium on 'Impact of Acoustic Loads on Aircraft Structures,'* Lillehammer, Norway. Acoustic fatigue behaviour of glare composites.
5. J. B. YOUNG *et al.* 1994 *Composite Structures* **27**, 457–469. Crack growth and residual strength characteristics of two grades of glass-reinforced aluminium 'glare'.
6. A. D. VLOT 1992 *SAMPE European Chapter*, 347–360. Low and high velocity impact loading of fibre/metal laminates, carbon/peek and monolithic aluminium 2024-T3.
7. N. OHRLOFF and P. HORST 1992 *SAMPE European Chapter*, 131–142. Feasibility study of the application of glare materials in wide body aircraft fuselage.
8. P. SMITH 1999 *Acoustic Fatigue of Aircraft Structures*. Meng: Aerospace Engineering *Institute of Sound and Vibration Research.*
9. R. G. WHITE 1978 *Composites* **9**, 251–258. A comparison of some statistical properties of the responses of aluminium and CFRP plates to acoustic excitation.
10. A. W. LEISSA 1969 *Vibration of plates, NASA SP*-160. Washington, DC: US Government Printing Office.
11. K. M. WHITNEY and A. W. LEISSA 1969 *American Society of Mechanical Engineers Journal of Applied Mechanics* **36**, 261–266. Analysis of heterogeneous anisotropic plates.
12. A. W. LEISSA 1973 *Journal of Sound and Vibration* **31**, 257–293. The free vibration of rectangular plates.
13. M. SATHYAMOORTHY 1987 *Appllied Mechanical Review* **40**, 1553–1561. Nonlinear vibration analysis of plates: a review and survey of current developments.
14. C. Y. CHIA 1980 *Nonlinear Analysis of Plates*. New York: McGraw-Hill.
15. C. Y. CHIA 1988 *Applied Mechanical Review* **41**, 439–451. Geometrically nonlinear behavior of composite plates: a review.
16. L. AZRAR, R. BENAMAR and H. F. WOLFE *Journal of Sound and Vibration*. Non-linear vibration analysis of beams and plates: a review of the literature and survey of methodological approaches. (to be submitted).
17. H. WOLFE 1995 Ph.D. *Thesis, University of Southampton, UK*. An experimental investigation of nonlinear behaviour of beams and plates excited to high levels of dynamic response.
18. R. G. WHITE 1971 *Journal of Sound and Vibration* **16**, 255–267. Effects of nonlinearity due to large deflections in the resonance testing of structures.
19. R. G. WHITE 1975 *Aero Journal* **79**, 318–325. Some measurements of the dynamic mechanical properties of mixed, carbon fibre reinforced plastic beams and plates.
20. R. G. WHITE, E. M. Y. ABDIN 1985 *Composites* **16**, 293–306. Dynamic properties of aligned short carbon fibre-reinforced plastic in flexure and torsion.
21. R. G. WHITE, R. F. MOUSLEY 1987 *Proceedings of the Fourth International Conference on Composite Structures, Paisley College of Technology*, July, 1519–1535. Dynamic response of CFRP plates under the action of random acoustic loading.
22. R. G. WHITE 1988 *Proceedings of the 25th AIAA/ASME Structures, Structural Dynamics and Materials Conference, Williamsburg*, USA, 253–260, Paper 88-2242. The acoustic excitation and fatigue of composite plates.
23. W. HAN and M. PETYT 1996 *Computers and structures* **61**, 705–712. Linear vibration analysis of laminated rectangular plates using the hierarchical finite element method—I: free vibration analysis.

24. W. HAN and M. PETYT 1996 *Computers and structures* **61**, 713–724. Linear vibration analysis of laminated rectangular plates using the hierarchical finite element method—II: forced vibration analysis.
25. W. HAN and M. PETYT 1997 *Computers and structures* **63**, 295–308. Geometrically nonlinear vibration analysis of thin, rectangular plates using the hierarchical finite element method—I: the fundamental mode of isotropic plates.
26. W. HAN and M. PETYT 1997 *Computers and structures* **63**, 295–308. Geometrically nonlinear vibration analysis of thin, rectangular plates using the hierarchical finite element method—II: 1st mode of laminated plates and higher modes of isotropic and laminated plates.
27. P. RIBEIRO and M. PETYT 1999 *International Journal of Mechanical Sciences* **41**, 437–459. Nonlinear vibration of plates by the hierarchical finite element and continuation methods.
28. P. RIBEIRO and M. PETYT 1999 *Journal of Sound and Vibration* **225**, 127–152. Multi-modal geometrical non-linear free vibration of fully clamped composite laminated plates.
29. R. BENAMAR, M. M. K. BENNOUNA and R. G. WHITE 1991 *Journal of Sound and Vibration* **149**, 179–195. The effects of large vibration amplitudes on the fundamental mode shape of thin elastic structures, Part I: simply supported and clamped–clamped beams.
30. R. BENAMAR, M. M. K. BENNOUNA and R. G. WHITE 1993 *Journal of Sound and Vibration* **164**, 295–316. The effects of large vibration amplitudes on the fundamental mode shape of thin elastic structures, Part II: fully clamped rectangular isotropic plates.
31. R. BENAMAR, M. M. K. BENNOUNA and R. G. WHITE 1990 *Proceedings of the Fourth International Conference on Recent Advances in Structural Dynamics, Southampton.* The effects of large vibration amplitudes on the fundamental mode shape of a fully clamped, symmetrically laminated rectangular plate.
32. F. MOUSSAOUI, R. BENAMAR and R. G. WHITE 2000 *Journal of Sound and Vibration* **232**, 917–943. The effect of large vibration amplitudes on the mode shapes and natural frequencies of thin elastic shells. Part I: coupled transverse–circumferential mode shapes of isotropic circular shells of infinite length.
33. R. BENAMAR, M. M. K. BENNOUNA and R. G. WHITE 1990 *Proceedings of the Eighth International Modal Analysis Conference*, Kissimmee, FL, 1352–1358. Spatial distribution of the harmonic distortion induced by large vibration amplitudes of fully clamped beams and rectangular plates.
34. R. BENAMAR, M. M. K. BENNOUNA and R. G. WHITE 1994 *Journal of Sound and Vibration* **175**, 377–424. The effects of large vibration amplitudes on the mode shapes and natural frequencies of thin elastic structures, Part III: fully clamped rectangular isotropic plates-measurements of the mode shape amplitude dependence and the spatial distribution of harmonic distortion.
35. M. EL KADIRI, R. BENAMAR and R. G. WHITE November 1999 *Journal of Sound and Vibration* **228**, 333–358. The non-linear free vibration of fully clamped rectangular plates: second non-linear mode for various plate aspect ratios.
36. L. AZRAR, R. BENAMAR and R. G. WHITE 1999 *Journal of Sound and Vibration* **224**, 183–207. A semi-analytical approach to the non-linear dynamic response problem S–S and C–C beams at large vibration amplitudes, Part I: general theory and application to the single mode approach to free and forced vibration analysis.
37. Z. BEIDOURI, R. BENAMAR and R. G. WHITE *Journal of Sound and Vibration.* The effects of large vibration amplitudes on the mode shapes and natural frequencies of C–C–C–SS rectangular isotropic plates (to be submitted).
38. M. HATERBOUCH, R. BENAMAR and R. G. WHITE *Journal of Sound and Vibration.* The effects of large vibration amplitudes on the mode shapes and natural frequencies of clamped circular isotropic plates (to be submitted).
39. B. HARRAS, R. BENAMAR and R. G. WHITE *Journal of Sound and Vibration.* Geometrically non-linear free vibration of fully clamped symmetrically laminated rectangular composite plates (to be published).
40. W. HAN 1993 *Ph.D. Thesis, Institute of Sound and Vibration Research.* The analysis of isotropic and laminated rectangular plates including geometrical non-linearity using the p-version finite element method.
41. J. T. BROCH 1980 *Mechanical Vibration and Shock Measurements.* Bruel & Kjaer.
42. S. KASTIS 1998 *M. Sc. Thesis, Institute of Sound and Vibration Research University of Southampton.* Acoustic fatigue of a new form of aircraft construction.
43. D. J. EWINS 1984 *Modal Testing: Theory and Practice.* England: *Research Studies Press Ltd*, New York: John Wiley and Sons Inc.
44. J. E. ASHTON and J. M. WHITNEY 1970 *Theory of Laminated Plates.* Borehamwood, UK: Technomic Publication.

45. TIMOSHENKO 1959 *Theory of Plates and Shells.* New York: McGraw-Hill, p. 416.
46. M. M. K. BENNOUNA and R. G. WHITE 1984 *Journal of Sound and Vibration* 309–331. The effects of large vibration amplitudes on the fundamental mode shape of a clamped–clamped uniform beam.
47. M. J. D. POWELL 1965 *Computer Journal* 7, 303–307. A method for minimising a sum of squares of non-linear functions without calculating derivatives.
48. R. G. WHITE 1990 *Composite Structures* **16**, 171–192. Developments in the acoustic fatigue design process for composite aircraft structures.

APPENDIX A

A.1. EXPRESSIONS OF THE NON-DIMENSIONAL TENSORS

m_{ij}, k_{ij} and b_{ijkl} are the mass tensor, the rigidity tensor and the geometrical non-linearity tensor respectively. The expressions for these tensors are

$$k_{ij} = \frac{aH^5 E}{b^3} k^*_{ij}, \quad b_{ijkl} = \frac{aH^5 E}{b^3} b^*_{ijkl}, \quad m_{ij} = \rho H^3 abm^*_{ij}, \tag{A.1–A.3}$$

where the non-dimensional tensors m^*_{ij}, k^*_{ij} and b^*_{ijkl} are given in terms of integrals of the non-dimensional basic functions w^*_i's, defined as in reference [39], and their first and second partial derivatives by

$$m^*_{ij} = \int_{S^*} w^*_i \, w^*_j \, \mathrm{d}x^* \, \mathrm{d}y^*, \tag{A.4}$$

$$\begin{aligned} k^*_{ij} = \int_{S^*} \Bigg\{ & D^*_{11}\,\alpha^4 \left[\frac{\partial_2 w^*_i}{\partial x^{*^2}} \frac{\partial_2 w^*_j}{\partial x^{*^2}}\right] + D^*_{22} \left[\frac{\partial_2 w^*_i}{\partial y^{*^2}} \frac{\partial_2 w^*_j}{\partial y^{*^2}}\right] \\ & + D^*_{12}\,\alpha^2 \left[\frac{\partial^2 w^*_i}{\partial x^{*^2}} \frac{\partial^2 w^*_j}{\partial y^{*^2}} + \frac{\partial^2 w^*_i}{\partial y^{*^2}} \frac{\partial^2 w^*_j}{\partial x^{*^2}}\right] + 2D^*_{16}\,\alpha^3 \left[\frac{\partial^2 w^*_i}{\partial x^{*^2}} \frac{\partial^2 w^*_j}{\partial x^* y^*} + \frac{\partial^2 w^*_i}{\partial x^* y^*} \frac{\partial^2 w^*_j}{\partial x^{*^2}}\right] \\ & + 2D^*_{26}\,\alpha \left[\frac{\partial^2 w^*_i}{\partial y^{*^2}} \frac{\partial^2 w^*_j}{\partial x^* y^*} + \frac{\partial^2 w^*_i}{\partial x^* \, y^*} \frac{\partial^2 w^*_j}{\partial y^{*^2}}\right] + 4D^*_{66}\,\alpha^4 \left[\frac{\partial^2 w^*_i}{\partial x^* y^*} \frac{\partial^2 w^*_j}{\partial x^* \, y^*}\right] \Bigg\} \mathrm{d}S^* \end{aligned} \tag{A.5}$$

$$\begin{aligned} b^*_{ijkl} = \int_{S^*} \Bigg\{ & \frac{A^*_{11}}{4}\,\alpha^4 \left[\frac{\partial w^*_i}{\partial x^*} \frac{\partial w^*_j}{\partial x^*} \frac{\partial w^*_k}{\partial x^*} \frac{\partial w^*_l}{\partial x^*}\right] + \frac{A^*_{22}}{4} \left[\frac{\partial w^*_i}{\partial y^*} \frac{\partial w^*_j}{\partial y^*} \frac{\partial w^*_k}{\partial y^*} \frac{\partial w^*_l}{\partial y^*}\right] \\ & + \left[\frac{A^*_{12}}{4} + \frac{A^*_{66}}{2}\right] \alpha^2 \left\{\left[\frac{\partial w^*_i}{\partial y^*} \frac{\partial w^*_j}{\partial y^*} \frac{\partial w^*_k}{\partial x^*} \frac{\partial w^*_l}{\partial x^*}\right] + \left[\frac{\partial w^*_i}{\partial x^*} \frac{\partial w^*_j}{\partial x^*} \frac{\partial w^*_k}{\partial y^*} \frac{\partial w^*_l}{\partial y^*}\right]\right\} \\ & + \frac{A^*_{16}}{4}\,\alpha^3 \left\{\left[\frac{\partial w^*_i}{\partial x^*} \frac{\partial w^*_j}{\partial x^*} \frac{\partial w^*_k}{\partial x^*} \frac{\partial w^*_l}{\partial y^*}\right] + \left[\frac{\partial w^*_i}{\partial x^*} \frac{\partial w^*_j}{\partial x^*} \frac{\partial w^*_k}{\partial y^*} \frac{\partial w^*_l}{\partial x^*}\right]\right\} \\ & + \frac{A^*_{26}}{2}\,\alpha \left\{\left[\frac{\partial w^*_i}{\partial x^*} \frac{\partial w^*_j}{\partial y^*} \frac{\partial w^*_k}{\partial y^*} \frac{\partial w^*_l}{\partial y^*}\right] + \frac{A^*_{22}}{4} \left[\frac{\partial w^*_i}{\partial y^*} \frac{\partial w^*_j}{\partial x^*} \frac{\partial w^*_k}{\partial y^*} \frac{\partial w^*_l}{\partial y^*}\right]\right\} \Bigg\} \mathrm{d}S^* \end{aligned} \tag{A.6}$$

$A_{ij}\,D_{ij}$ are the coefficients of the symmetric matrices A and D respectively. They are given by

$$(A_{ij}, B_{ij}, D_{ij}) = \int_{-H/2}^{H/2} Q^{(k)}_{ij}\,(1,\, z,\, z^2)\,(\mathrm{d}z), \tag{A.7}$$

where the $Q^{(k)}_{ij}$ are the reduced stiffness coefficients of the kth layer in the plate co-ordinates. $A^*_{ij} = (A_{ij}/HE)$ and $D^*_{ij} = (D_{ij}/H^3E)$, in which H is the plate thickness and E is a reference Young's modulus, whose numerical value was taken as 7×10^{10} N/m, which is a typical value for aluminium alloys.

A.2. NUMERICAL DETAILS OF THE FULLY CLAMPED SYMMETRICALLY LAMINATED RECTANGULAR PLATE ANALYSIS

A.2.1. Plate functions used

The chosen basic functions f_i^{a*} were the linear clamped–clamped beam functions [30]:

$$f_i^{a*}(x) = \frac{[ch(v_i\,x/L) - \cos(v_i x/L)]}{(chv_i - \cos v_i)} - \frac{[sh(v_i\,x/L) - \sin(v_i x/L)]}{(shv_i - \sin v_i)}, \tag{A.8}$$

where v_i for $i = 1, 2, \ldots$ are the eigenvalue parameters for a clamped–clamped beam. The values of the parameters v_i were computed by solving numerically the transcendental equation $\cosh v_i \cos v_i = 1$ and are given in reference [39].

The fully clamped rectangular plate functions w_i^* were defined as

$$w_i^*(x^*, y^*) = \frac{1}{G}\, f_{\alpha i}^{a*}(x^*)\, f_{\beta i}^{a*}(y^*) \tag{A.9}$$

in which $x^* = x/L$, $y^* = y/L$, $w_i^*(x^*, y^*) = w_i/H\,(x/L, y/L)$ and G is a normalization scaling factor given by

$$G = \sqrt{\int_{S^*} (f_{\alpha i}^{a*}(x^*) f_{\beta i}^{a*}(y^*))^2 \,\mathrm{d}x^*\,\mathrm{d}y^*}\,. \tag{A.10}$$

The functions w_i were normalized in such manner that

$$m_{ij}^* = \int_0^1 w_i^*(x^*)\, w_j^*(x^*)\,\mathrm{d}x^* = \delta_{ij}. \tag{A.11}$$

A.2.2. Details of the application of Hamilton's principle

The dynamic behaviour of the structure is governed by Hamilton's principle, which is symbolically written as

$$\partial \int_0^{2\pi/\omega} (V - T) = 0 \tag{A.12}$$

in which δ indicates the variation of the integral. Introducing the assumed series (14) into the energy conditions (A.12) via equation (15) reduces the problem to that of finding the minimum of the function ϕ given by

$$\phi = \int_0^{2\pi/\omega} \left(\frac{1}{2}\, a_i a_j k_{ij}^* \sin^2 \omega t + \frac{1}{2}\, a_i a_j a_k a_l b_{ijkl}^* \sin^4 \omega t - \frac{1}{2}\, \omega^2 a_i a_j m_{ij}^* \cos^2 \omega t \right) \mathrm{d}t \tag{A.13}$$

with respect to the undetermined constant a_i. Integrating the trigonometric functions $\sin^2 \omega t$, $\sin^4 \omega t$ and $\cos^2 \omega t$ over the range $[0, 2\pi/\omega]$ leads to the following expression:

$$\phi = \frac{\pi}{2\omega} \left(a_i a_j\, k_{ij}^* + \frac{3}{4} a_i a_j\, a_k\, a_l\, b_{ijkl}^* - \omega^2 a_i a_j m_{ij}^* \right). \tag{A.14}$$

In this expression, ϕ appears as a function of only the undetermined constant, a_i, $i = 1, \ldots, n$. Equation (A.12) reduces to

$$\frac{\partial \phi}{\partial a_r} = 0, \quad r = 1, \ldots, n, \tag{A.15}$$

which can be written as

$$\frac{2\pi}{\omega}\left(\frac{\partial a_i}{\partial a_r} a_j k^*_{ij} + a_i \frac{\partial a_j}{\partial a_r} k^*_{ij} + \frac{3}{4}\frac{\partial a_i}{\partial a_r} a_j a_k a_l b^*_{ijkl} + \frac{3}{4} a_i \frac{\partial a_j}{\partial a_r} a_k a_l b^*_{ijkl} + \frac{3}{4} a_i a_j \frac{\partial a_k}{\partial a_r} a_l b^*_{ijkl}\right.$$

$$\left. + \frac{3}{4} a_i a_j a_k \frac{\partial a_l}{\partial a_r} b^*_{ijkl} - \omega^2 \left(\frac{\partial a_i}{\partial a_r} a_j m^*_{ij} + a_i \frac{\partial a_j}{\partial a_r} m^*_{ij}\right)\right) = 0, \quad r = 1, \ldots, n. \tag{A.16}$$

As we have

$$\frac{\partial a_i}{\partial a_r} = \delta_{ir}, \quad \frac{\partial a_j}{\partial a_r} = \delta_{jr}, \quad \frac{\partial a_k}{\partial a_r} = \delta_{kr}, \quad \frac{\partial a_l}{\partial a_r} = \delta_{lr}, \tag{A.17}$$

where δ is the Kronecker symbol defined by $\delta_{ij} = 1$ if $i = j$ and $\delta_{ij} = 0$ if $i \neq j$, equations (A.16) lead to

$$(a_j k^*_{ij} + a_i k^*_{ij}) + \frac{3}{4}(a_j a_k a_l b^*_{ijkl} + a_i a_k a_l b^*_{ijkl} + a_i a_j a_l b^*_{ijkl} + a_i a_j a_k b^*_{ijkl})$$

$$- \omega^2 (a_j m^*_{ij} + a_i m^*_{ij}) = 0, \quad r = 1, \ldots, n \tag{A.18}$$

Generally, and this is case for all the applications of this theory given in reference [48], and presented in this present work, the tensors k^*_{ij} and m^*_{ij} are symmetric, and the tensor b^*_{ijkl} is such that:

$$b^*_{ijkl} = b^*_{klij} \text{ and } b^*_{ijkl} = b^*_{jikl}. \tag{A.19}$$

Taking into account these properties of symmetry, it appears that equations (A.18) are equivalent to the following set of non-linear algebraic equations:

$$2 a_i k^*_{ir} + 3 a_i a_j a_k b^*_{ijkr} - 2\omega^2 a_i m^*_{ir} = 0, \quad r = 1, \ldots, n. \tag{A.20}$$

A.2.3. Symmetrization procedure for the bending and non-linear rigidity tensors k^*_{ij} and b^*_{ijkl}

A.2.3.1. Illustration of the symmetrization procedure. Consider the bending strain energy (expression (11)). The discretization of terms proportional to D_{11}, D_{22} and D_{66} leads to symmetric expressions with respect to *i* and *j*; but the discretization of the other terms leads to expressions which need to be symmetrized in order to obtain a symmetric rigidity matrix k^*_{ij}. For example, the discretization of the term

$$2D_{12}\frac{\partial^2 W}{\partial y^2}\frac{\partial^2 W}{\partial x^2} \tag{A.21}$$

leads to

$$2D_{12} a_i a_j \frac{\partial^2 w_i}{\partial y^2}\frac{\partial^2 w_j}{\partial x^2}. \tag{A.22}$$

If only two different given values are assigned to the indices *i* and *j*, the expression obtained is not symmetric. But, expression (A.22) involves a summation over the repeated indices *i* and *j*. So, it may also be written as

$$2D_{12} a_i a_j \times \frac{1}{2}\left[\frac{\partial^2 w^*_i}{\partial y^{*^2}}\frac{\partial^2 w^*_j}{\partial x^{*^2}} + \frac{\partial^2 w^*_i}{\partial x^{*^2}}\frac{\partial^2 w^*_j}{\partial y^{*^2}}\right]. \tag{A.23}$$

This is the form adopted in equations (A.5) for this term.

A similar procedure has been adopted for the other terms, in order to obtain s symmetric rigidity tensor. Also, a similar procedure has been applied when discretizing the non-linear axial strain energy V_a in order to fulfil the symmetry requirements $b^*_{ijkl} = b_{klij}$ and $b^*_{ijkl} = b^*_{jikl}$.

APPENDIX B: CALIBRATION OF THE MEASUREMENT SYSTEM

Before undertaking experimental measurements, some necessary calibrations have been done in order to check the instruments and experimental set-up. It was necessary to know

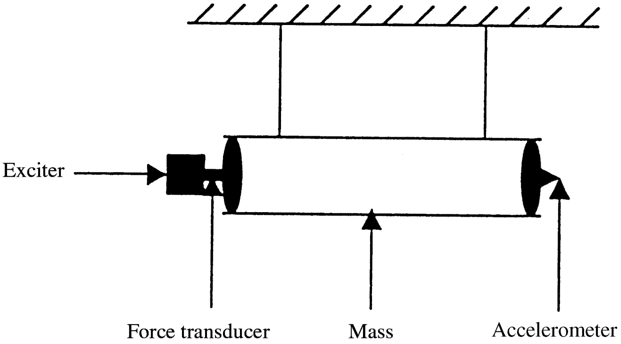

Figure B1. Accelerometer and force transducer calibration.

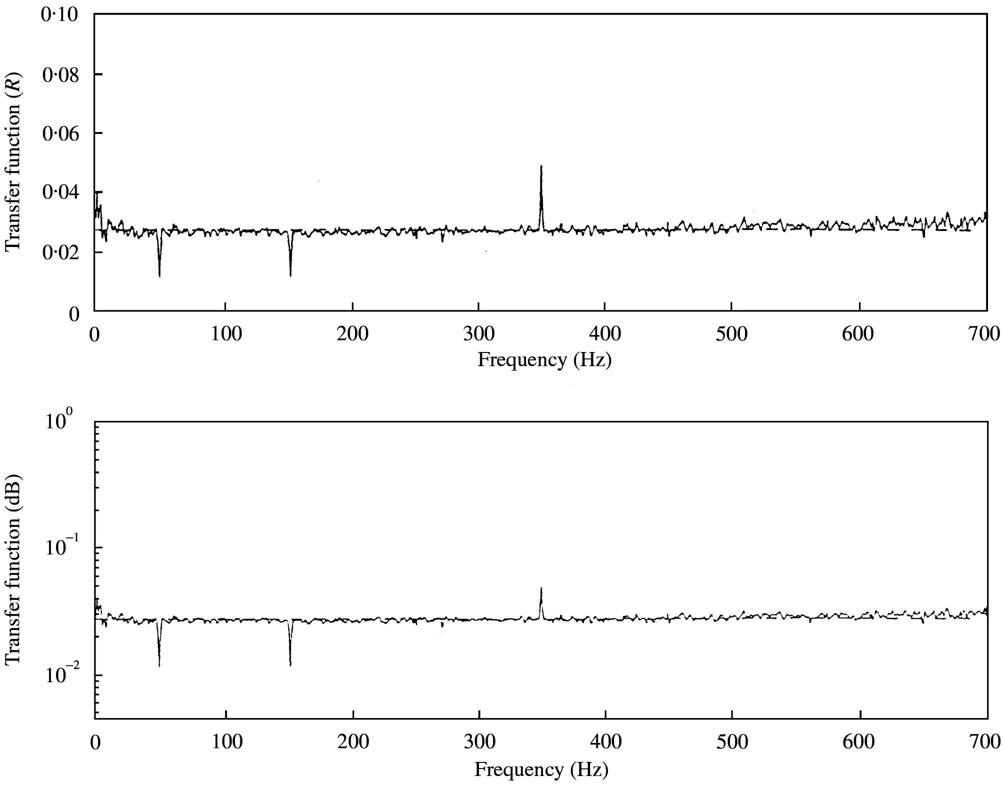

Figure B2. Calibration of the transducers for the modal tests of the Glare 3 hybrid composite panel (upper—linear scale; lower—logarithmic scale).

the sensitivites of the transducers used, in order to obtain accurate results during the measurements of the transfer functions. For this work, the accelerometer and force transducer were used. However, it is important to calibrate those transducers before beginning any measurements. The sensitivity of a transducer might change after being used for some time and other instruments might also induce errors. The indirect calibration method was used because it is difficult to measure the sensitivity of each individual transducer. This method may be described as follows.

A cylindrical mass was suspended on a wire, and an accelerometer and vibration exciter were attached at each end of the mass as shown in Figure B1. The relationship between the excitation force f and the response acceleration "a" of mass "m" should follow Newton's law: "$f = ma$". The transfer function therefore can be expressed as "$a/f = 1/m$", in the frequency range concerned. Figure B2 shows the calibration result of the transducers for the modal tests of the G3HCRP. The relation between a/f and $1/m$ represents the overall sensitivity S (m/s^2/N). This means that the transfer function (accelerance) a/f is given by $(a/f)_m/S$, where $(a/f)_m$ is the measured transfer function. For the modal tests, only the transfer functions are of interest and this calibration method is satisfactory. For the transducers used in this work, the overall sensitivity was 0·01 (m/s^2/N).

APPENDIX C: NOMENCLATURE

$\{\boldsymbol{\varepsilon}\}$	column matrix of total strains
$\{\boldsymbol{\varepsilon}^0\}$	column matrix of strains due to the in-plane displacements u, v, w
x, y, z	point co-ordinates
$\{\boldsymbol{\kappa}\}$	column matrix of bending or twisting
$\{\boldsymbol{\lambda}^0\}$	column matrix of strains induced by large displacements W
ε_x, ε_y, γ_{xy}	tensors strain components
$\sigma_x^{(k)}$, $\sigma_y^{(k)}$, $\sigma_{xy}^{(k)}$	stresses in the kth layer
$[\mathbf{Q}]$	6×6 matrix of transformed stiffness
$[\mathbf{Q}]_k$	6×6 matrix of transformed stiffness for the kth layer
$N_x^{(k)}$, $N_y^{(k)}$, $N_{x,y}^{(k)}$	force resultant for the kth layer
$M_x^{(k)}$, $M_y^{(k)}$, $M_{x,y}^{(k)}$	moment resultant for the kth layer
h_k	distance from the mid-plane to the layer surface of the kth layer
A_{ij}, B_{ij}, D_{ij}	extensional, coupling and bending stiffness coefficients for the laminate plate
A_{ij}^*, D_{ij}^*	non-dimensional extensional and bending stiffness coefficients
a_{ij}	contribution coefficient of the plate deflection function as a product of the ith and jth beam model shapes in the x and y directions respectively
a, b	length, width of the plate
E	Young's modulus
H	plate thickness
k_{ij}, m_{ij} and b_{ijkl}	general term of the rigidity tensor, the mass tensor and the non-linearity tensor respectively
k_{ij}^*, m_{ij}^* and b_{ijkl}^*	general term of the non-dimensional rigidity tensor, mass tensor and non-linearity tensor respectively
S, S^*	dimensional and non-dimensional surfaces $[0, a] \times [0, b]$ and $[0, 1] \times [0, 1]$ respectively
$U(x, y, t)$, $V(x, y, t)$	in-plane displacements at point (x, y) of the plate $U(x, y, t) = u(x, y) \sin^2 \omega t$ $V(x, y, t) = v(x, y) \sin^2 \omega t$
V_b, V_a and V	bending, axial and total strain energy respectively
T	kinetic energy
$W(x, y, t)$	transverse displacement at point x on the plate $W(x, y, t) = w(x, y) \sin \omega t$
$W^*(x, y, t)$	non-dimensional transverse displacement at point x on the plate
w_{max}^*	maximum of the non-dimensional transverse displacement

a_k	contribution corresponding to the *k*th basic functions
w_k	*k*th basic spatial function.
α	non-dimensional parameter (aspect ratio) given by $\alpha = a/b$
v_{xy}	major Poisson ratio
E_x	longitudinal modulus
E_y	transverse modulus
G_{xy}	shear modulus
m	cylindrical mass
S	overall sensitivity
ρ	mass density per unit volume of the plate
ω, ω^*	frequency and non-dimensional frequency parameters respectively
ω_l, ω_{nl}	linear frequency and non-linear frequency parameters respectively
σ_{xh}, σ_{yh}	dimensional bending stresses
σ^*_{xh}, σ^*_{yh}	non-dimensional dimensional bending stresses.